Very low-grade metamorphism of the Dezadeash flysch (Jura-Cretaceous): Constraints on the burial history of the Nutzotin-Dezadeash basin and implications regarding the tectonic evolution of the Northern Cordillera of Alaska and Yukon

Grant W. Lowey

Whitehorse, Yukon

Corresponding Author: Grant Lowey (loweygrant@gmail.com)

Key Points:

* mineralogic and organic thermal indicators record mainly high temperature zeolite facies metamorphism, diagenetic to anchizone metapelitic conditions, and catagenesis to metagenesis thermal maturation stages
* the thermal history, subsidence history, and secondary mineral assemblages do not support peripheral foreland, backarc, strike-slip, or rift basin settings
* unlike the contemporaneous Gravina belt and Gravina sequence in southeast Alaska, the Dezadeash formation was not underthrust to > 20 km beneath the Yukon composite terrane

Abstract

Secondary mineral assemblages in sandstone and tuff indicate high temperature zeolite facies metamorphism; Kübler indices of illite and Árkai indices of chlorite in mudstone record diagenetic to high anchizone metapelitic conditions; and pyrolysis of organic matter and the color of organic matter (i.e., the Thermal Alteration Index of palynomorphs and the Conodont Alteration Index) in mudstone and hemipelagite beds suggest thermal maturation reached catagenesis to mesogenesis stages. Collectively, the mineralogic and organic thermal indicators suggest the Dezadeash Formation was subject to pressure-temperature (P-T) conditions of 2.5 kbar and 250 °C. The estimated P-T conditions, together with published thermochronometric data, shows that the Dezadeash Formation underwent rapid, short-term heating followed by gradual, long-term cooling. Moreover, a calculated tectonic subsidence curve indicates rapid, short-term subsidence, followed by gradual, long-term uplift. Secondary clay minerals associated with heating and subsidence are characterized by a restricted assemblage dominated by $2M_1$ illite and chlorite. The thermal history, subsidence history, and secondary clay mineral assemblage are not supportive of deposition in peripheral foreland, backarc, strike-slip, and rift basins; nor are the results corroborative with previous deformation and crustal-scale reconstructions depicting the Dezadeash Formation being underthrust >20 km beneath the Blanchard River assemblage, Kluane Schist, and Yukon composite terrane (YCT). The Dezadeash-Nutzotin basin contrasts sharply with the contemporaneous Gravina belt and Gravina sequence in southeastern Alaska that were apparently underthrust >20 km beneath the YCT. The contrasting tectono-metamorphic histories may be a manifestation of oblique collision and diachronous, south-to-north accretion of the Chitina arc and WCT to YTC.

1. Introduction

The Mesozoic convergence and subsequent collision of the Wrangellia composite terrane with the western margin of Laurasia was accompanied by the formation of several flysch basins. The flysch basins are preserved as relatively thick, variably deformed Jurassic-Cretaceous sedimentary and volcanic rocks scattered along the Northern Cordillera of Alaska and Yukon (Fig. 1). Conflicting basin settings have been proposed for these Jurassic-Cretaceous sedimentary and volcanic rocks, including: backarc basins (Berg et al., 1972; Plafker et al., 1989; Cohen and Lundberg, 1993; Monger et al., 1994; Gehrels et al., 2009; Yokelson et al., 2015); intra-arc basins (Berg et al., 1972; McClelland et al., 1991; van der Heyden, 1992; Trop and Ridgway, 2007); forearc basins (Moore and Connelly, 1979; Gehrels and Berg, 1994; Trop and Ridgway, 2007; Lowey, 2019), retroarc foreland basins (Trop et al., 2002; Manuszak et al., 2007; Trop and Ridgway, 2007; Hampton et al., 2010); collisional foreland basins (Trop and Ridgway, 2007); remnant ocean basins (Nokleberg et al., 1985; Ridgway et al., 2002; Trop and Ridgway, 2007; Hampton et al., 2010), transtensional basins (McClelland et al., 1992; Cohen and Lundberg, 1993; Anderson, 2015); and rift basins (Brew and Ford, 1983). The spate of inferred basins is due in part to the paucity of matter-of-fact constraints on basin position and type: previous research focused mainly on determining depositional environments and provenance of the Jurassic-Cretaceous rocks, but depositional environments are generally non-unique with regards to basin type and tectonic setting (Reading, 1980; MacDonald, 1993; Dalrymple, 2010). Furthermore, provenance studies utilizing the framework mode of sandstones tend to provide only generalized and overlapping “provenance terranes” reflecting a variety of tectonic settings (Dickinson and Suczek, 1979; Dickinson et al., 1983; Boggs, 2009), whereas provenance studies relying on detrital zircon geochronology may result in the misidentification of potential source

terranes (and hence tectonic settings) due to biases in data manipulation related to discordance filters, concealed lead loss, and common lead correction (Anderson, et al., 2019), as well as biases resulting from differential igneous zircon fertility, sediment sorting, and preservation potential compared with other detrital minerals such as monazite (Moecher and Sampson, 2006; Hietpas et al., 2010; Ibañez-Mejia et al., 2018).

Plate tectonics exerts a first-order control on the basin fill because the tectonic setting determines the local geothermal gradient, subsidence mechanism, sediment accumulation rate, available mineral and rock fragment composition, pore fluid composition, water circulation (i.e., porosity and permeability), and general basin type (Siever, 1979; Blatt, 1992). Hence, additional constraints on the type of basin and its tectonic setting may be obtained by analysing the post-depositional history of the basin fill, specifically determining diagenetic zones, metamorphic facies, thermal history, and subsidence history of strata comprising the basin. For example, Merriman (2002, 2005) utilized diagenetic and metamorphic clay mineral assemblages to infer the tectonic setting of sedimentary basins: mudstones that evolved in extensional basins contained a complex assemblage of clay minerals comprising K-, Na/K-, Na-micas and pyrophyllite, as well as chlorite/mica stacks, compared with mudstones that evolved in convergent basins that displayed a simple clay mineral assemblage of K-white mica and chlorite. In addition, Xie and Heller (2009) employed tectonic subsidence curves to distinguish between passive margin, strike-slip, and foreland basins: subsidence histories record isostatic adjustment to lithospheric processes such as thermal events and sediment loading, and tectonic subsidence curves reflect basin subsidence caused exclusively by a tectonic or driving mechanism, calculated by removing subsidence produced by non-tectonic processes such as compaction and

sediment loading (i.e., "backstripping"), as well as water depth changes (Bond and Kominz, 1984).

Temperature is possibly the most important parameter affecting the basin fill since it influences many of the post-depositional physical properties of sediments and pore fluids, and basin thermal histories are thought to be indicative of tectonic setting and associated basins (Allen and Allen, 2013). Consequently, Stone and Merriman (2004) proposed that a "basin thermal history test" be undertaken as part of any terrane analysis, particularly collapsed flysch basins comprising thick, variably deformed strata for which the tectonic setting is ambiguous. A basin thermal history test attempts to distinguish between basins with normal or near-normal paleogeothermal gradients, commonly associated with passive margins, oceanic trenches, forearc, and foreland basins, from hotter-than-normal paleogeothermal gradients typical of backarc, rift, and lithospheric-scale strike-slip basins (Stone and Merriman, 2004; Allen and Allen, 2013). The thermal history of a sedimentary basin can be inferred from a variety of low-temperature geothermometers, such as: temperature-sensitive quartz and calcite microstructures (Weber et al., 2001); homogenization temperatures of fluid inclusions that indicate the minimum temperature of entrapment of the fluid (Randive et al., 2014); kinetically independent thermal indicators such as authigenic clay mineral assemblages and dispersed organic matter that furnish a maximum paleotemperature of the material examined (Hartkopf-Fröder et al., 2015); K-Ar dating of diagenetic illite that provides the time the mineral precipitated (Meunier et al., 2004); and apatite and zircon fission track analyses that reveal both the time and temperature of formation of the mineral analyzed (Reiners and Ehlers , 2005).

This paper presents the results of an integrated thermal history analysis of the Dezadeash Formation, including: structural fabrics observed in outcrop; petrographic examination of thin

sections of sandstones, mudstone, hemipelagite, and volcaniclastic beds; X-ray diffraction of sandstone, mudstone, hemipelagite, and volcaniclastic beds, including whole-rock, clay speciation, and illite Kübler index and chlorite Árkel index "crystallinity" determinations; microfossil analysis of mudstone and hemipelagite beds for palynomorphs and limestone clasts for conodonts; and pyrolysis maturation analysis of mudstones and hemipelagites. Published thermochronometric data from the Dezadeash Formation are also incorporated. In addition, the paper presents the results of a quantitative subsidence analysis, including sediment decompaction and backstripping. The primary aim of this contribution is to characterize the post-depositional alteration of the Dezadeash Formation in an attempt to determine the maximum temperature and pressure reached by the strata. The goal is to constrain the burial history of the Nutzotin-Dezadeash basin, which may have implications regarding the tectonic evolution of the Northern Cordillera of Alaska and Yukon with respect to basin type and tectonic setting.

2. Geologic Setting

The northern Cordillera and adjoining areas are an amalgamation of allochthonous composite terranes, superimposed magmatic arcs, and exhumed sedimentary flysch basins, all variably offset by lithospheric-scale strike-slip faults. Geologic elements relevant to this study include: the Yukon, Wrangellia, and South Margin composite terranes; the Chitina, Chisana, and Kluane arcs; the Gravina, Dezadeash, Nutzotin, Wrangell, Blanchard River, and Kluane Schist basins; and the Border Ranges, Fairweather, Denali, and Coast-Tatshenshini faults.

2.1. Composite terranes

2.1.1. Yukon composite terrane

The Yukon composite terrane (YCT) refers to the polymetamorphosed and polydeformed Yukon-Tanana, Slide Mountain, Cache Creek, Quesnellia, and Stikinia terranes (Fig. 1) (Wheeler and McFeely, 1991; Monger, 2014). The YCT includes a substrate of Proterozoic to Paleozoic metasedimentary and mafic meta-igneous rocks, overlain by an assemblage of Devonian-Mississippian arc-related volcanic and sedimentary rocks (Plafker and Berg, 1994; Nelson et al., 2013). The YCT was rifted from the ancient margin of North America in the middle Paleozoic, resulting in the formation of the oceanic Slide Mountain terrane, and subsequently re-attached to North America in the latest Paleozoic (Nelson et al., 2013). The Cache Creek terrane is a subduction-related assemblage that is flanked by late Paleozoic to early Mesozoic volcanic arc rocks belonging to Quesnellia and Stikinia (Monger, 2014). Final accretion of the YTC to the western margin of Laurentia occurred in the mid-Cretaceous (Monger et al., 1982; Monger and Journeay, 1994; Nelson et al., 2013).

2.1.2. Wrangellia composite terrane

The Wrangellia composite terrane (WCT) is an amalgamation of three tectonostratigraphic terranes referred to as the Alexander, Wrangellia, and Peninsular terranes (Fig. 1) (Plafker and Berg, 1994). The Alexander terrane includes a basement of Neoproterozoic to early Paleozoic island arc-related volcanic and sedimentary rocks (Nokleberg et al., 1994; Beranek et al., 2012), and also late Paleozoic island arc-related volcanic and sedimentary rocks. The Wrangellia terrane consists mainly of late Paleozoic to early Mesozoic island arc-related volcanic and sedimentary rocks. The Peninsular terrane consists of an assemblage of Mesozoic arc-related volcanic rocks (Nokleberg et al., 1994). The three terranes represent successively higher structural and stratigraphic successions from southeast to northwest (Nokleberg et al.,

1994). The Alexander and Wrangellia terranes were contiguous during the late Paleozoic, based on Pennsylvanian-age plutons that intrude both terranes (Gardner et al., 1988). The Peninsular terrane collided in Late Jurassic time with either the western margin of Laurasia (the Yukon composite terrane), or the combined Alexander-Wrangellia terrane (Clift et al., 2005; Beranek et al., 2014). The WCT, interpreted as part of an obliquely converging oceanic plateau (Greene et al., 2010), was emplaced against the margin of Laurasia during the mid-Jurassic to mid-Cretaceous (Monger et al., 1982; McClelland et al., 1992a; Nokleberg et al., 1994).

2.1.3. South Margin composite terrane

The South Margin composite terrane (SMCT) includes the Mesozoic Chugach terrane and the Cenozoic Prince William terrane (Fig. 1) (Trop and Ridgway, 2007). These two terranes comprise metamorphic rocks and offscraped oceanic sedimentary and volcanic rocks interpreted as a subduction complex (Plafker et al., 1994). The SMCT is in contact with the WCT along the Border Ranges fault (Fig. 1). The Border Ranges fault, inferred as an Early Jurassic to Late Cretaceous subduction zone megathrust, is thought record large magnitude dextral slip (possibly > 500 km) since Late Cretaceous-Paleogene time (Pavlis and Roeske, 2007).

The Southern Margin composite terrane is flanked to the south by the Yakutat terrane. (Fig. 1). The Yakutat terrane is interpreted as a displaced fragment of the western North America continental margin that was transported ~600 km along the Fairweather fault (Fig. 1) (Plafker and Berg, 1994). Subduction of the Yakutat terrane beneath North America began ~30 Ma ago and is ongoing; the subduction is partly responsible for major uplift of the St. Elias Mountains syntaxis and exhumation of the Dezadeash Formation (Plafker and Berg, 1994; Enkelmann et al., 2017; McDermott et al., 2019).

2.2. Arcs and Basins

The number of magmatic arcs, their polarity, and the tectonic setting of contemporaneous sedimentary basins in the northern Cordillera is controvertible (Saleeby, 1983; Hildebrand, 2013; Shepard et al., 2013; Gehrels et al., 2017; Lowey, 2017; Sigloch and Mihalynuk, 2017; Pavlis et al., 2019; Chen et al., 2019; Zhang et al., 2019; Fu et al., 2020). Therefore, this section presents a detailed description of these Jurassic-Cretaceous rocks.

2.2.1. Late Jurassic-Early Cretaceous

Manifestations of the Chitina arc (~160–140 Ma; Plafker et al., 1989; Nokleberg et al., 1994; Roeske et al., 1991, 2003) are scattered from southeastern Alaska, through southwestern Yukon, and into southcentral Alaska (Fig. 1) (Nokleberg et al., 1994). In southeastern Alaska, metavolcanic rocks interpreted as pillowed to massive basaltic to andesitic lava flows, basaltic breccia, and crystal-rich volcaniclastics dominate the lower part of the Gravina sequence (Fig. 2) (Rubin and Saleeby, 1991). Minor amounts of metasedimentary rocks (mainly conglomerate and mudstone) are also present and are considered Late Jurassic in age based on the bivalve *Buchia* (Rubin and Saleeby, 1991). Major, trace and rare earth element geochemistry indicates that the volcanic rocks resemble modern island arc tholeiites (Rubin and Saleeby, 1991). According to Rubin and Saleeby (1991), the lower unit unconformably overlies the Alexander terrane and has a structural thickness of ~1300 m. The lower volcanic unit is depositionally overlain by an upper metasedimentary unit comprising tuffaceous turbidites, mudstone-sandstone turbidites, and conglomerate (Fig. 2). The upper unit has a structural thickness of ~900 m and contains granitic clasts with U-Pb zircon ages ranging from 154–158 Ma (Rubin and Saleeby, 1991). Rubin and

Saleeby (1991) interpreted the lower unit as lava flows shed from the flanks of submarine volcanoes and the upper unit as submarine fans deposited adjacent to dissected volcanic centers; they concluded that the Gravina sequence represents the remnants of an island arc with a contemporaneous sedimentary cover that accumulated on the eastern (inboard) edge of the Alexander terrane. In contrast, Yokelson et al. (2015) proposed that, on the basis of U-Pb and Hf isotope analyses of detrital zircons, the Gravina sequence represents an "eastern facies" which accumulated along the western margin of the YCT. The Gravina sequence is structurally overlain by the YCT and experienced greenschist to amphibolite facies metamorphism (Rubin and Saleeby, 1992).

Volcanic and volcaniclastic rocks derived from the Chitina arc occur also at the base of the Gravina belt in southeastern Alaska (Fig. 1 and 2). The volcanic and volcaniclastic rocks are inferred to be Late Jurassic in age and to depositionally overlie the Alexander terrane (McClelland et al., 1991). McClelland et al. (1991) reported that the volcanic rocks consist mainly of basaltic to andesitic flows that are geochemically similar to volcanic rocks at the base of the Gravina sequence. Lesser amounts of pyroclastic breccias, fine-grained volcaniclastics, and sandstone-mudstone turbidites are also present (McClelland et al., 1991). The basal volcanic rocks of the Gravina belt are locally overlain conformably by the Seymour Canal Formation (Fig. 2) (Gehrels, 2000). The Seymour Canal Formation is ~1800 m thick succession dominated by sandstone and mudstone turbidites with minor amounts of conglomerate (Lanthram et al., 1965; McClelland et al., 1991; Cohen, 1992; Gehrels, 2000). Sandstones contain detrital biotite that reveal $^{40}Ar/^{39}Ar$ ages of ~159–129 Ma (Cohen et al., 1995), and the strata are considered to be Late Jurassic (Oxfordian) to Early Cretaceous (Albian) in age based on the bivalve *Buchia* (Lanthram et al., 1965; Gehrels, 2000). The Seymour Canal Formation also locally overlies

unconformably the Alexander terrane (Cohen, 1992; Cohen and Lundberg, 1993). The Seymour Canal Formation is interpreted as upper and middle submarine fan deposits sourced from the WCT (Cohen, 1992; Gehrels, 2000; Gehrels et al., 2009). Haeussler (1992) noted that sandstones from the unit display prehnite-pumpellyite facies metamorphism, whereas associated volcanic rocks display greenschist to amphibolite facies metamorphism. Cohen and Lundberg (1993) observed that the Seymour Canal Formation is regionally metamorphosed to zeolite, prehnite-pumpellyite, and lower-greenschist facies in the north, increasing to greenschist facies in the south. The Seymour Canal Formation is conformably overlain by the Douglas Island Volcanics and Brothers Volcanics (Lanthram et al., 1965), correlative with the Chisana arc describe later.

Volcaniclastic rocks derived from the Chitina arc occur in the Dezadeash Formation in southwest Yukon (Fig. 1 and 2), the focus of this study. Three thick volcaniclastic beds (measuring 9.7, 8.5 and 1.5 m thick from the lowest to highest bed) consisting of fine-to medium-grained vitric to crystal tuff are interpreted as resedimented syn-eruptive volcaniclastic gravity flow deposits (Lowey, 2011). A U-Pb zircon age of 149.4 ±0.3 Ma indicates they are contemporaneous with the Chitina arc, and a variety of tectonic discriminant diagrams show they have a continental arc signature, which Lowey (2011) attributed to the WCT proxying for continental crust.

The Dezadeash Formation is an approximately 3000 m thick succession of thin- to thick-bedded turbidites and massive sandstone with minor amounts of conglomeratic mudstone containing limestone clasts up to ~10 m in exposed longest dimensions, volcaniclastic rocks, and hemipelagic lime mudstone (Eisbacher, 1976; Lowey, 1992, 2007). Based on detailed lithofacies analysis, the Dezadeash Formation represents mainly the middle and lower subdivisions of a

point-source, mud/sand-rich submarine fan (Lowey, 2007) that was derived from the WCT and Chitina arc (Lowey, 2019).

The Dezadeash Formation is Late Jurassic (Oxfordian) to Early Cretaceous (Valanginian) in age based on collections of the bivalve *Buchia* (Eisbacher, 1976), and uncomfortably overlies the Alexander and Wrangellia terranes, specifically Triassic volcanic, volcaniclastic, and carbonate rocks belonging to the Nikolai Formation, McCarthy Formation, and Chitistone and Nisina Limestone (Dodds and Campbell, 1992a). The Dezadeash Formation is overlain unconformably by ~1000 m of unmetamorphosed nonmarine Paleogene clastic and volcaniclastic rocks of the Amphitheater Formation (Eisbacher, 1976; Ridgway et al., 1995).

Eisbacher (1976) identified two phases of folding in the Dezadeash Formation: the oldest folds (F_1) trend northerly, are asymmetric or overturned to the east, and locally change laterally into thrust faults; the youngest folds (F_2) trend west-northwesterly and are open. The oldest folds are crosscut by the Shorty Creek pluton that reveals a K-Ar age of ~106 Ma (Dodds and Campbell, 1988). Eisbacher (1976) attributed the oldest folds to movement on a "tectonic slope" because the trend of the folds is similar to the trend of penecontemporaneous slump folds in the Dezadeash Formation; he ascribed the youngest folds to westward directed thrusting of the Kluane Schist over the Dezadeash Formation and movement on the Denali fault zone. Both the Kluane Schist and Denali fault are described later.

Metamorphism of the Dezadeash Formation is poorly documented. Sturrock (1975) concluded that strata had undergone prehnite-pumpellyite facies burial metamorphism, but this was based on the examination of a single thin section from the contact aureole of the Pyroxenite Creek complex (Cretaceous). And Dodds and Campbell (1992b) noted in the legend of the geologic map of the Dezadeash area that the Dezadeash Formation was "unmetamorphosed to

regionally metamorphosed up to subgreenschist facies (laumontite-prehnite-quartz)", but provided no additional information on how this determination was reached.

The Dezadeash Formation has also been utilized in low-temperature thermochronometric investigations. Specifically, two samples by Enkelmann et al. (2017) and possibly one sample by McDermott et al. (2019) from the St. Elias Mountains syntaxis in southwest Yukon (Fig. 3), are summarized in Table 1. The thermochronometric investigations reveal multiple episodes of exhumation and landscape evolution, which McDermott et al. (2019) attribute to rapid cooling at ~95–75 Ma due to accretion of the WCT to the YCT, slow cooling during ~75–30 Ma caused by relief degradation, and renewed rapid cooling beginning ~30 Ma and continuing to the present, attributed to flat-slab subduction of the Yakutat terrane and strike-slip displacement on the Denali fault zone.

Volcaniclastic rocks likely derived from the Chitina arc have been reported from the Nutzotin Mountains sequence in southcentral Alaska (Fig. 1 and 2), but the volcaniclastic rocks have not been described in detail, nor have they been radiometrically dated (Richter, 1976). The Nutzotin Mountains sequence is up to 3000 m thick and consists mainly of thin-bedded turbidites with minor amounts of massive sandstone, conglomeratic mudstone (containing limestone clasts up to ~10 m exposed longest dimensions), and hemipelagite beds (Berg et al., 1972; Richter, 1976; Kozinski, 1985; Manuszak et al., 2007). The strata are interpreted as westerly sourced, distal to proximal submarine fan deposits that grade upward into shelf deposits (Kozinski, 1985; Manuszak et al., 2007). The Nutzotin Mountains sequence is Late Jurassic (Tithonian) to Early Cretaceous (Valanginian) in age and unconformably overlies the Wrangellia terrane (Manuszak and Ridgway, 2000). The strata are deformed by north-dipping thrust faults and overturned folds

that are crosscut by 117–105 Ma plutons, and is conformably overlain by the mainly volcanic Chisana Formation (Manuszak et al., 2007).

Metamorphism of the Nutzotin Mountains sequence is also poorly documented. Kozinski, (1985) measured two stratigraphic sections in the northeastern part of the Nutzotin Mountains sequence that are separated by ~6 km. Observing prehnite in a thin section from one of the measured sequences and discovering pumpellyite in a thin section from the second measured sequence, Kozinski (1985) concluded that the Nutzotin Mountains sequence had undergone prehnite-pumpellyite grade metamorphism. And Dusel-Bacon et al. (1993) indicated in the explanation of a map of regionally metamorphose rocks of Alaska that the Nutzotin Mountains sequence was “unmetamorphosed”.

Eisbacher (1976) proposed that the Dezadeash Formation and Nutzotin Mountains sequence represent the same strata that was dismembered and displaced by the Denali fault system (Eisbacher, 1976). The Denali fault system is one of the main strike-slip faults in the Northern Cordillera, along which ~370 km of dextral slip occurred since the Early Cretaceous (Clague, 1979; Lowey, 1998, and references therein). Sedimentologic and stratigraphic studies by Kozinski (1985), Manuszak (2000), and Manuszak and Ridgway (2000) on the Nutzotin Mountains sequence, and Lowey (2019) on the Dezadeash Formation corroborates this interpretation.

Volcanic rocks of the Chitina arc likely also occur in the Wrangell Mountains basin of south-central Alaska (Fig. 1 and 2). The Wrangell Mountains basin is comprised of three depositional sequences each bounded by unconformities: the lower sequence consists of ~1700 m of mudstone, sandstone, and conglomerate (i.e., Root Glacier Formations and Kotsina Conglomerate) that is Late Jurassic (Kimmeridgian-Tithonian) in age; the middle sequence

consists of ~300 m of calcareous sandstone and mudstone (i.e., Berg Creek and Kuskulana formations) that is Early Cretaceous (Hauterivian-Barremian) in age; and the upper sequence consists ~3575 m of sandstone, conglomerate, and mudstone, with minor porcellanite and rare tuff (i.e., Kennicott, Moonshine Creek, Schultze, Chititu, and MacColl Ridge formations) that is Early to Late Cretaceous (Albian-Campanian) in age (MacKevitt, 1971; Trop et al., 2002). The lower sequence rests unconformably on the WCT, and the upper sequence is unconformably overlain by siliciclastic rocks (Fredrika Formation) and volcanic rocks (Wrangell Lava) that are Miocene to Pliocene in age (Trop et al., 2002). In the lower sequence, thin bedded aphanitic flows and vitric tuffs are interbedded with mudstone and sandstone of the ~1100 m thick Root Glacier Formation (Trop et al., 2002). The volcanic and volcaniclastic rocks have not been described in detail, nor have they been radiometrically dated. The Root Glacier Formation is Early Jurassic (Oxfordian-Tithonian) in age, and is interpreted as submarine slope and fan deposits sourced from the WCT (Trop and Ridgway, 2007). Strata appear to be unmetamorphosed (MacKevett, 1971; Trop et al., 2002).

Plutonic rocks interpreted as the roots of the Chitina arc extend from southeastern Alaska, through southwestern Yukon and into southcentral Alaska. The plutonic rocks occur as elongate batholithic complexes to smaller single and multiple phase plutons that are widespread, and generally decrease in size, abundance, mafic composition and possibly depth of emplacement from west to east (Dodds and Campbell, 1988; Hudson, 1983; Plafker et al., 1989). The intrusions are commonly parallel to regional trends, exhibit abrupt to gradational boundaries, and are locally foliated (Dodds and Campbell, 1988; Hudson, 1983). The rocks are calk-alkaline in composition and consist mainly of quartz diorite, tonalite and granodiorite ranging from Late Jurassic to Early Cretaceous in age (~160–130 Ma) (Dodds and Campbell, 1988; Hudson,1983;

342 Miller, 1994; Plafker et al., 1989; Roeske et al., 1991). The batholiths and plutons include the
343 Tonsina–Chichagof belt of Hudson (1983) and the Saint Elias plutonic suite of Dodds and
344 Campbell (1988). They correspond to the 160–140 Ma period of magmatic flux summarized by
345 Gehrels et al. (2009) for the Northern Cordillera. The Chitina arc is restricted to the Wrangell
346 and Alexander terranes of the WCT (Fig. 1), and there are no conclusive data to constrain the
347 polarity of subduction of the arc (Plafker et al., 1989; Monger and Price, 2002).
348 Trop and Ridgway (2007) proposed that the Chitina arc represents the eastern extension
349 of the Talkeetna arc ('T' in Fig. 1). However, volcanism associated with the Talkeetna arc ended
350 during Early to Middle Jurassic time (~180–170 Ma) (Rioux et al., 2007), before initiation of
351 Chitina arc volcanism in Late Jurassic time (~150 Ma). In addition, the Talkeetna arc is
352 interpreted as an archetypal example of an intraoceanic arc and is mainly restricted to the
353 Peninsular terrane (Rioux et al., 2007), whereas the Chitina arc displays continental margin arc
354 signatures and is confined to the Wrangellia and Alexander terranes (Lowey, 2011). Polarity of
355 the Talkeetna arc is debatable (Reed et al., 1983; Trop and Ridgway, 2007)
356

357 ### 2.2.2. Early Cretaceous

358 The Chisana arc (~120–105 Ma; Short et al, 2005; Falkowski and Enkelman, 2016) is
359 represented by the Douglas Island Volcanics and Brothers Volcanics in southeastern Alaska, and
360 the Chisana Formation in southcentral Alaska (Fig. 1 and 2). In southeastern Alaska, the Douglas
361 Island Volcanics and Brothers Volcanics conformably overly the Gravina belt (specifically the
362 Seymour Canal Formation) (Lanthram et al., 1965). The volcanic units are dominated by augite
363 porphyritic basalt characterized as breccia and pillowed flows, and minor amounts of
364 volcaniclastics and mudstone-sandstone turbidites (Lanthram et al., 1965; Gehrels, 2000).

Geochemically, the volcanic rocks are calc-alkaline and related to a volcanic arc and subduction zone setting (Stowell et al., 2000). The Douglas Island/Brothers Volcanics are ~300–600 m thick and are considered Early Cretaceous in age (mainly Hauterivian to possibly Albian) (Lanthram et al., 1965; Gehrels, 2000). The Douglas Island Volcanics experienced prehnite-pumpellyite to greenschist facies metamorphism with pressure-temperature (P-T) estimated to have reached 2–7.5 kbars and 325 °C (Himmelberg et al., 1995). The Douglas Island Volcanics are conformably overlain by sandstone, mudstone, and conglomerate assigned to the Treadwell Formation that has a detrital zircon inferred maximum depositional age of ~105 Ma (Gehrels, 2000).

The Gravina belt (i.e., Seymour Canal Formation, Douglas Island and Brothers Volcanics, and Treadwell Formation) is structurally overlain by the YCT to the east (Fig. 1). Stowell and Crawford (2000) summarized the metamorphic history of the Gravina belt and recognized that the earliest metamorphic event as regional in extent (i.e., M_1^R) and characterized by low- to moderate-pressure (2–6 kbar) and low temperature (~150–275 °C). In contrast, McClelland and Mattinson (2000) postulated that parts of the belt were underthrust to deep crustal levels of 25–30 km.

The Chisana Formation (Fig. 2) gradationally overlies the Nutzotin Mountains sequence in southcentral Alaska. The Chisana Formation includes a lower unit of mainly basaltic and andesitic flows and minor amounts of sandstone, mudstone, and volcaniclastic rocks up to ~1100 m thick, and an upper unit of interlayered volcanic-lithic breccia, basaltic-andesite flows, conglomerate, and mudstone, and volcaniclastic rocks up to ~2500 m thick (Berg et al., 1972; Richter, 1976; Barker, 1987; Manselle et al., 2020). The formation is Late Cretaceous in age (Aptian-Albian) based on $^{40}Ar/^{39}Ar$ ages of ~116–113 Ma (Short et al., 2005). The unit is interpreted to have been deposited proximal to volcanic vents on subaqueous (lower unit) and

388 subaerial (upper unit) slopes of the contemporaneous proto-continental, or intraoceanic Chisana
389 arc (Short et al., 2005; Manselle et al., 2020). The Chisana Formation appears to have been
390 subject to unspecified subgreenschist facies metamorphism (Berg et al., 1972; Manselle et al.,
391 2020), and is unconformably overlain by the unmetamorphosed Beaver Lake Formation, a ~90 m
392 thick assemblage of Early to Late Cretaceous conglomerate, tuff and coal deposited in fluvial
393 systems (Manselle et al., 2020).

394 Other Early Cretaceous flysch basins contemporaneous with the Chisana arc include the
395 Wrangell Mountain basin in south-central Alaska and the Blanchard River assemblage in
396 southwestern Yukon (Fig.1 and 2). In the Wrangell Mountains basin, calcareous sandstone and
397 mudstone of the Berg Creek and Kuskulana formations are Early Cretaceous (Hauterivian-
398 Barremian, 132-121 Ma) in age and restricted to the western half of the basin (Trop et al., 2002).
399 The Blanchard River assemblage consists mainly of interlayered quartz-biotite schist and quartz-
400 biotite psammitic schist that grades eastward into proto-gneiss and paragneiss before becoming
401 engulfed by the Ruby Range batholith (~64–54 Ma) of the Coast Plutonic Complex (Vice, 2017).
402 According to Vice (2017), the Blanchard River assemblage is ~5000–6000 m thick with a
403 detrital zircon based maximum depositional age of 130–125 Ma. The zircons are inconclusive
404 with regards to provenance and suggest derivation from either the YCT, the WCT, or both, and it
405 is unknown if the Blanchard River assemblage was deposited on WCT or YCT crust (Vice,
406 2017). The Blanchard river assemblage is structurally overlain by the YCT, and reached
407 amphibolite facies metamorphism with P-T conditions estimated to have been ~6.5 kbars (~24
408 km depth) and ~640°C (Vice, 2017).

409 Plutonic rocks interpreted as the roots of the Chisana arc extend from southeastern
410 Alaska, through southwestern Yukon and into southcentral Alaska. The plutonic rocks occur as

411 elongate batholithic complexes and plutons of granodiorite, quartz diorite, diorite, and rarer
412 quartz monzonite (Dodds and Campbell, 1988). The rocks are calk-alkaline in composition and
413 are Early Cretaceous in age (~117–106 Ma) (Dodds and Campbell, 1988; Hudson,1983; Miller,
414 1994; Plafker et al., 1989; Roeske et al., 1991). The batholiths and plutons include the Nutzotin-
415 Chichagof belt (120–105 Ma) belt of Hudson (1983) and the Muir-Chichagof belt of Brew and
416 Morrell (1983) in Alaska, and the Kluane Ranges plutonic suite of Dodds and Campbell (1988)
417 in southwest Yukon. The Shorty Creek pluton of the Kluane Ranges plutonic suite intrudes the
418 Dezadeash Formation (Fig. 2) and has a K-Ar age of ~106 Ma (Dodds and Campbell, 1988).
419 Roots of the Chisana arc are also preserved as Alaskan-type ultramafic complexes,
420 specifically the Klukwan-Duke belt in southeast Alaska (Brew and Morrell, 1983), and the
421 Pyroxenite Creek complex in southwestern Yukon (Fig. 3) (Dodds and Campbell, 1988). The
422 Pyroxenite Creek complex intrudes the Dezadeash Formation and has K-Ar ages of ~128–109
423 Ma and a Rb-Sr age of ~116 Ma (Rb-Sr) (Sturrock et al., 1980). According to Sturrock (1975),
424 the intrusion resulted in a 30 m wide contact metamorphic aureole of albite-epidote hornfels
425 facies in the Dezadeash Formation.
426 The Chisana arc is restricted to the Wrangell and Alexander terranes of the WCT (Fig.1),
427 and is included in of the 120–78 Ma period of magmatic flux summarized by Gehrels et al.
428 (2009) for the Northern Cordillera. There are no conclusive data to constrain the polarity of
429 subduction of the arc, although subduction is generally assumed to be northeastward (Plafker et
430 al., 1989; Monger and Price, 2002)
431
432
433

2.2.3. Late Cretaceous-Paleogene (Eocene)

Volcaniclastic rocks likely derived from the Kluane arc (~85–45 Ma, Nokleberg et al., 2000; Amato et al., 2007) also occur in the Wrangell Mountain basin in southcentral Alaska (Fig. 1 and 2). In the uppermost sequence, tuff is interbedded with ~1150 m of sandstone, conglomerate, and mudstone of the MacColl Ridge Formation (Trop et al., 2002). Vitric tuff beds measuring 10–100 cm thick reveal $^{40}Ar/^{39}Ar$ ages of ~80–76 Ma (Stamatakos et al., 2001), contemporaneous with the Kluane arc. The MacColl Ridge Formation is Late Cretaceous (Campanian) in age, and is interpreted as submarine fan deposits sourced from the WCT (Trop and Ridgway, 2007). Strata appear to be unmetamorphosed (MacKevett, 1971; Trop et al., 2002).

Other Early Cretaceous basins contemporaneous with the Kluane arc include the Kluane Schist in southwestern Yukon (Fig.1 and 2). The Kluane Schist is a sequence of graphitic mica–chlorite–quartz schist and gneiss with a structural thickness of ~12,000 m that contains interfoliated bodies of serpentinized dunite up to 1.5×15 km in exposed dimensions (Mezger et al., 2001a). Zircon geochronology indicates the protolith of the Kluane Schist is Late Cretaceous in age (<94 Ma) (Stanley, 2012), although Tempelman-Kluit (1976) reports a K-Ar biotite age of 140 Ma. It is not known if the Kluane Schist was sourced from the WCT, the YCT, or both, and whether the unit was deposited on WCT or YCT crust (Mezger et al., 2001a; Canil et al. (2015). The Kluane Schist is structurally overlain by the YCT and was subject to greenschist to amphibolite facies metamorphism with P-T estimated to have been 7 kbar (~24 km depth) and 500 °C (Tempelman-Kluit, 1976; Mezger et al., 2001a).

Plutonic rocks interpreted as the roots of the Kluane arc form part of the extensive Coast Plutonic Complex, or Coast Mountains Batholith (~175–45 Ma, Armstrong, 1988; Gehrels et al.,

2009) that extends for much of the length of the Northern Cordillera and into east-central Alaska (Fig. 1). The Coast Plutonic Complex is inferred to have formed immediately after accretion of the WCT with the YCT (i.e., the ancient margin of western North America) and the intrusive complex obscures the "Shakwak" suture between these two composite terranes (Eisbacher, 1985; Amato et al., 2007). The roots of the Kluane arc are preserved mainly as calk-alkaline diorite, quartz diorite, granodiorite and locally monzonite, and syenite plutons that intrude both the WCT and the YCT (Plafker et al., 1989). The Kluane arc is interpreted as part of a continental-margin arc that was active during the Late Cretaceous and Paleogene (Plafker et al., 1989; Nokleberg et al., 1994; Plafker and Berg, 1994; Monger and Nokleberg, 1996). The Kluane arc overlaps the periods of high magnetic flux of 120–78 Ma and 55–48 Ma and the magnetic lull of 78–55 Ma of Gehrels et al. (2009). There are no conclusive data to constrain the polarity of subduction of the arc, although subduction is generally assumed to be northeastward (Plafker et al., 1989; Monger and Price, 2002).

Intimately associated with the Coast Plutonic Complex is the Coast shear zone (Fig.1). The Coast shear zone, as defined by Andronicos et al. (1999) and Chardon et al. (1999), consists of the Great Tonalite Sill (located along the western margin of the Coast Mountains Complex) and related flanking structures extending more than 1000 km from southern British Columbia into southeastern Alaska (Fig. 1). Displacement across the Coast shear zone is dominantly east-over-west and this occurred in mid-Cretaceous time (Brew, 1997; Brew and Ford, 1998; Stowell and Hooper, 1990; McClelland et al., 1992b; Andronicos et al., 1999; Chardon et al., 1999); the Great Tonalite Sill is interpreted as a synkinematic sill intruding the shear zone (Stowell and Hooper, 1990; McClelland et al., 1992; Ingram and Hutton, 1994; Brew and Ford, 1998; Klepeis et al., 1998; Andronicos et al., 1999; Chardon et al., 1999). McClelland and Mattinson (2000)

proposed that the Coast shear zone may have originated as a lithospheric strike-slip fault that accommodated 300-600 km dextral translation.

Stowell and Crawford (2000) determined that emplacement of Coast Plutonic Complex sill plutons along the Coast shear zone next to the Gravina belt resulted in contact metamorphism (M_4^C) characterized by sillimanite-zone assemblages indicating moderate pressure (~6 kbar) and high temperature (700 °C). Lowey (2000) extended the Coast Shear zone into southwest Yukon as part of the Tatshenshini shear zone (Fig. 1). The Tatshenshini shear zone is characterized by protomylonitic and mylonitic turbidites of the Dezadeash Formation in the footwall and protomylonitic granodiorite of the Ruby Range Batholith (part of the Coast Plutonic Complex) in the hangingwall (Lowey, 2000). Kinematic indicators from the Dezadeash Formation and Ruby Range Batholith record a top-to-the southwest sense of shear. A whole rock K-Ar age of 60.2 ±1.9 Ma obtained from mylonite indicates that the main phase of shearing took place no later than ~60 Ma ago. Initial emplacement of the Ruby Range Batholith along the Tatshenshini shear zone appears to have occurred ~75–68 Ma ago. The intrusion resulted in contact metamorphism of the Dezadeash Formation that is characterized by andalusite-chiastolite poikiloblastic phyllite with a K-Ar age of 68.2 ±1.8 Ma (Lowey, 2000); the intrusion was apparently shallow and reached ~490 °C (Mezger, 1997).

Stowell et al. (2000) concluded that metamorphism and emplacement of Coast Plutonic Complex in the Gravina belt resulted in an average geothermal gradient of < 20 °C/km at ~100 Ma, and likely closer to <14 °C/km (Stowell and Crawford, 2000). Stowell and Crawford (2000) suggested that these inferred geothermal gradients are not compatible with a rift setting for the Gravina belt because such a setting would be characterized by a higher heat flow and a higher temperature of metamorphism.

3. Methods

This study is based on 16,335 m of measured strata from 75 sections throughout the Dezadeash Formation (Fig. 3 and Supplementary Table S1). In addition to collecting standard bed-by-bed sedimentological measurements (i.e., bed thickness, lithology, grain size, and sedimentary structures), data was also collected pertaining to secondary deformation features (i.e., cleavage, folds, joints, and veins). Approximately 200 samples were collected from these sections, and a subset of samples from the 200 initially collected were selected for analysis.

Seventy-two samples were selected for thin-section analysis, including 35 sandstone, 4 coquina, 11 mudstone, 7 hemipelagite, and 15 tuff samples. Standard thin sections, half of which were impregnated with blue epoxy, and standard off-cuts, all of which were stained for potassium feldspars, were prepared by Vancouver Petrographics Ltd., Langley, British Columbia. The thin-sections were examined by transmitted light microscopy with a standard petrographic microscope.

Eight samples of were selected for processing for palynomorphs (spores and pollen). The samples were prepared following standard extraction techniques (Traverse, 1988), including disaggregation and washing, HCl and HF acid digestion, oxidation with Schulze's solution, and separation of the organic fraction from the heavier residue with $ZnCl_2$. The organic fraction was mounted on glass slides with liquid bioplastic and examined with a transmitted light microscope using oil immersion at 400x and 1000x magnification. The degree of maturation of the organic fraction, basically the thermally induced, systematic and irreversible changes in the color of the organic material, was determined by visual comparison with the Thermal Alteration Index of Staplin (1969). The Thermal Alteration Index (TAI) is a semi-quantitative numerical scale from

1 to 5, with 1 being the lower maturity light color (i.e., colorless to light yellow) and 5 being the more mature darker color (i.e., black with indications of metamorphism) (Staplin, 1969).

One limestone clast was selected for conodont analysis and separated using standard acetic acid processing techniques by the Geological Survey of Canada, Vancouver, British Columbia. A discussion of the procedure is provided by Harris and Sweet (1989) and Orchard and Foster (1991). The degree of maturation of the recovered conodonts was determined by visual comparison with the Conodont Alteration Index (Epstein et al., 1977). The Conodont Alteration Index (CAI) is also a semi-quantitative numerical scale from 1 to 5, similar in principle to the TAI, with 1 corresponding to a lower maturity light color (i.e., clear or colorless) and 5 corresponding to a more mature darker color (i.e., black) (Epstein et al., 1977).

Two samples of sandstone and one sample each of hemipelagite and tuff were submitted to AGAT Laboratories Ltd., Calgary Alberta, for quantitative X-ray diffraction analysis including clay speciation, and scanning electron microscope (SEM) and energy dispersive X-ray (EDX) analyses. The quantitative XRD analysis was performed on the bulk sample and clay fraction. The clay fraction (less than 2 μm size) was separated from the bulk sample by centrifuging. The samples were treated in an ultrasonic bath using sodium hexametaphosphate as a deflocculating agent to facilitated complete disintegration of the matrix from the grains. Samples were centrifuged in two phases. In the first phase, the samples were centrifuged at 600 rpm for 5 minutes to enable coarser particles to settle to the bottom of the tube. Clay particles remaining in fluid suspension were decanted into another tube, and for the second phase centrifuged at 3000 rpm for 45 minutes. The clay fraction was mounted on glass slides and placed in glycol vapor bath for 24 hours in order to identify expandable clays. Weight fractions were measured for both bulk and clay portions of the samples. Step-scan X-ray powder-

549 diffraction data was collected over a range of 3–80º2θ with CoKα radiation on a standard
550 Siemens (Bruker) D5000 Bragg-Brentano diffractometer equipped with a Fe monochromator
551 foil, 0.6 mm (0.3º) divergence slit, incident- and diffracted-beam Sollers slits and a Vantec-1
552 strip detector. The long fine-focus Co X-ray tube was operated at 35 kV and 40 mA, using a
553 take-off angle of 6º. The X-ray diffractograms were analyzed using the International Center for
554 Diffraction database PDF-4 using Search-Match software by Siemens (Bruker). For SEM
555 analysis, a piece of each sample was glued on to aluminum stubs and after lightly blowing off
556 loose particles with air, the samples were coated with gold to facilitate observations and
557 photography. The gold-coated samples were examined with a scanning electron microscope to
558 highlight the distribution and morphology of minerals. EDX analysis was also carried out to
559 determine elemental compositions of minerals.
560 Two mudstone samples were submitted to Activation laboratories Ltd., Ancaster, Ontario
561 for quantitative XRD analysis including clay speciation. The quantitative XRD analysis was
562 performed on the clay fraction of the sample. A portion of each sample was pulverized, mixed
563 with corundum and packed into a standard holder. Corundum was used as an internal standard.
564 For the clay speciation analysis, a portion of each sample was dispersed in distilled water and
565 clay minerals in the < 2 μm size fraction separated by gravity settling of particles in suspension.
566 Oriented slides of the < 2 μm size fraction were prepared by placing a portion of the suspension
567 onto a glass slide. The oriented slides were analyzed air-dried, after treatment with ethylene
568 glycol and after heating at 375 °C for 1 hour. The XRD analysis was performed on a Panalytical
569 X'Pert Pro diffractometer equipped with Cu X-ray source and an X'Celerator detector and
570 operating at the following conditions: 40 kV and 40 mA; range 5–70° 2θ for random specimens
571 and 4–30° 2θ for oriented specimens; step size 0.017° 2θ; time per step 30 sec; fixed divergence

slit angle 0.25°. The X'Pert HighScore plus software along with the PDF4/Minerals ICDD database were used for mineral identification. The quantities of the crystalline mineral phases were determined using Rietveld method. The Rietveld method is based on the calculation of the full diffraction pattern from crystal structure data. The amounts of the crystalline minerals were recalculated based on a known percent of corundum and the remainder to 100 % was considered X-ray amorphous material. The Kübler Index (KI) was determined for illite in the < 2 μm size fraction following the procedure described by Kisch (1991): the full width of the peak at half the maximum peak height (FWHM) of the 10 Å-illite-peak was measured from the X-ray diffractogram in units of Δ°2θ CuKα radiation. Similarly, the Árkai Index (AI) was determined for chlorite in the < 2 μm size fraction following the method described by Árkai (1991): the FWHM of the 14 Å-chlorite-peak was measured from the X-ray diffractogram in units of Δ°2θ CuKα radiation. Both KI and AI measure the sharpness of the diffractogram peaks; the sharpness of the peaks is an indication of the crystallinity of the clay minerals, which provide an indication of the extent of diagenesis and metamorphism.

Twenty-three samples were selected for pyrolysis analysis. The samples were submitted to the Geological Survey of Canada in Calgary, Alberta, and analyzed using a Rock-Eval 6 Turbo (RE 6) instrument. This instrument uses a ramped temperature technique whereby a small amount of sample (70–100 mg) is heated in an inert atmosphere (helium or nitrogen) and also combusted with air to obtain several key geochemical parameters relating to the thermal maturation of the rock. Parameters important to this study include the total organic carbon (TOC wt %) in the sample, and the instrument oven temperature (T_{max} °C) at which the maximum quantity of hydrocarbons (S_2) generated by pyrolitic degradation of kerogen in the sample occurs. TOC is a measure of the utility of the analysis (<0.3 wt.% TOC suggests all parameters

595 have questionable significance), and T_{max} is a measure of the thermal maturation of the sample
596 (Peters, 1986). Two calculated parameters applicable to the study are the hydrogen index (HI)
597 and the oxygen index (OI). HI is a measure of the amount of hydrogen in the sample and is
598 calculated as HI =(S_2x100/TOC); and OI is a measure of the amount of oxygen in the sample and
599 is calculated as OI=(S_3x100/TOC), where S_3 represents the carbon dioxide generated during
600 pyrolysis (Behar et al., 2001). Plots of HI versus OI indicate the type of kerogen present:
601 generally, high HI and low to intermediate OI values indicate lacustrine organic matter (Type I
602 or Algal/Sapropelic) and mixed marine-terrestrial organic matter (Type II or planktonic),
603 whereas low HI values and moderate to low OI values indicate woody terrestrial organic matter
604 (Type III or humic) and degraded organic matter (Type IV or inert) (Behar et al., 2001). Details
605 of the Rock-Eval apparatus, procedures and applications are available in Lafargue et al. (1998)
606 and Behar et al. (2001).

607 Quantitative subsidence analysis followed the procedures outlined by van Hite (1978),
608 Angevine et al. (1990), and Allen and Allen (2013). A one-dimensional, local isostatic Airy
609 model was assumed for the analysis, and decompaction and backstripping formulas presented in
610 Angevine et al. (1990) were used. Subsidence analysis produces a sedimentation rate for the
611 decompacted basin fill and a basin subsidence curve due solely to tectonic forces. The tectonic
612 subsidence curve depicts the subsidence history of the basin, and this can be used to evaluate the
613 veracity of the thermal history of the basin determine via mineral and organic thermal indicators.
614 The shape of the tectonic subsidence curve may also be useful in delimiting the basin type (Xie
615 and Heller, 2009; Allen and Allen, 2013).

616

617

3. RESULTS

3.1. Field relationships

Well-exposed outcrops of the Dezadeash Formation occur throughout the St. Elias Mountains in southwestern Yukon. The majority of the outcrops are dominated by thin- to thick-bedded sandstone–mudstone couplets that form packets up to ~335 m thick, and medium- to thick-bedded sandstone that form amalgamated units up to ~136 m thick. Well preserved primary sedimentary structures are common in these lithologies, including erosional structures (sole marks and small channels), depositional structures (graded bedding, planar-stratification, and cross-stratification), deformation structures (load and flame structures, convolute stratification, dish and pillar structures, and slump structures), and biogenic sedimentary structures comprising sparse bioturbation with few discrete trace fossils preserved in the interior of beds and on the soles of beds. Detailed descriptions of these sedimentary structures and their distribution are presented in Eisbacher (1976) and Lowey (1980, 2007). The pristine nature of the sedimentary structures provided unambiguous evidence for the way-up of strata, and slump folds overlain by undeformed beds confirm that the slumps are due to soft-sediment movement and not a later tectonic deformation.

Superimposed on the primary sedimentary structures are a variety of secondary structures. Sandstone beds in thin- to medium-bedded sandstones-mudstone couplets locally display a sub-vertical parting (Fig. 4A). The parting is spaced 5–30 cm apart with a mean spacing of ~10.2 cm. Parting planes are parallel to each other and can be traced from one sandstone bed into several overlying or underlying sandstone beds, but they are not present in thick-bedded sandstone beds. Although the parting resembles a poorly developed spaced

642 cleavage, the mean ratio of the separation of the partings to the thickness of the beds (s/l) is
643 ~0.95. According to Hancock (1982), s/l >0.05 belong to a joint set.
644 Mudstones are characterized by a poorly developed parting or diagenetic foliation (cf.
645 Passchier and Trouw, 1996) that is sub-parallel to bedding (Fig. 4B). The diagenetic foliation is
646 moderately to strongly developed, parallel to curviplanar, and generally spaced 3–8 mm,
647 although up to 20 mm spacing is also present. The diagenetic foliation is associated with a
648 weakly to strongly developed spaced cleavage that is at a high-angle to bedding. The cleavage
649 domains have a spacing of 5–85 mm and are smooth, occupy <1% of the rock volume and are
650 parallel to curviplanar to each other. The intersection of the diagenetic foliation and spaced
651 cleavage results in mudstones weathering into angular, irregularly-shaped pebble-sized clasts.
652 Locally, mudstones display a moderately to well-developed spaced cleavage (Passchier and
653 Trouw, 1996). The cleavage domains have a spacing of 1–5 mm and are smooth, occupy <1% of
654 the rock volume and are parallel to each other (Fig. 4C). The spaced cleavage is associated with
655 the oldest folds (F_1) recognized by Eisbacher (1976). The F_1 folds have amplitudes ranging from
656 10's-100's m, are asymmetric to overturned to the east, and are cross-cut by the ~106 Ma Shorty
657 Creek pluton (Fig. 3). The spaced cleavage appears to be roughly axial planar, and both the
658 spaced cleavage and F_1 folds trend northerly. Rarely, well developed pencil structure (Passchier
659 and Trouw, 1996) is also present in the mudstone (Fig. 4D). The pencil structure, formed by the
660 intersection of well-developed diagenetic cleavage and spaced cleavage (S_0-S_1), trends
661 northwesterly, parallel to the F_1 folds. The pencil length varies from 49.5–164.2 mm and the
662 width ranges from 2.25–11.25 mm, with a mean shape factor (length-to-width ratio, L/W) of
663 14.5. A plot of the length and width of the pencils suggests a shortening of 9–26% (Fig. 5).

Hemipelagite beds display an irregular jointing spaced 10–20 cm (Fig. 4E), resulting in the beds weathering into angular, block-shaped cobble-sized clasts. Volcaniclastic beds display a more regular jointing spaced 20–50 cm that is intersected by a very irregular second joint set that is sub-parallel to bedding (Fig. 4F). As a result, the volcaniclastic beds weather into angular, irregularly-shaped boulder-sized clasts.

Several types of veins are locally present in the thin- to medium-bedded sandstones-mudstone couplets. The more common type of veining are swarms of veins that cross-cut bedding at various angles. The veins occur as differently oriented sets, often forming prominent networks, with sub-parallel veins regularly spaced ~10–20 cm. The veins are ~0.5–6 cm wide and syntaxial, with one or more phases of white quartz and minor amounts of calcite present that impart a banded appearance to the veins. Occasionally associated with the vein swarms are randomly oriented irregular vein masses, ptygma-like veins, and veinlets of milky white quartz. A less common type of veining are isolated veins and sets of veins parallel to bedding. The veins are ~4–8 cm wide and syntaxial, with a single phase of massive white quartz growing out from the wall rock of the vein.

3.2. Petrography

3.2.1. Sandstone

Sandstones consist manly of fine- to coarse-grained sand that is clast-supported and moderately to well sorted. Grains are subangular to sub-rounded, and grain boundaries tend to be indistinct, with mainly longitudinal to concavo-convex contacts and rare sutured contacts. Overall, the sandstones are characterized by a poorly developed fitted grain fabric (i.e., “complete” grain contacts, c.f., Wolf and Chilingarian, 1976). Sandstones are very pale brown

(10YR 7/4; Munsell Color Chart, 1994) to pale brown (10YR 6/3) in transmitted light at 35x magnification. Most grains have a thin black (5Y 2.5/2) rim in transmitted light at 35x magnification. When viewed at 500x magnification, the rim consists of minute, subhedral, semi-transparent olive (5Y 4/3) crystals. The remainder of the grain interstices (i.e., other interstitial material including matrix and cement), representing to ~5–15% of the area in thin sections, are dark grayish brown (10YR 4/2) at 35x magnification in transmitted light. There is no visible pore space.

Detailed petrography of the framework mode of sandstones can be found in Lowey (2019). Sandstones are characterized by a dominance of lithic fragments and are classified as litharenites to feldspathic litharenites (~$Q_{12}F_{26}L_{62}$) (Lowey, 2019). Lithic fragments include mainly volcanic grains, with minor amounts sedimentary lithic grains (chert, limestone, and mudstone), and rare metamorphic lithic fragments (phyllite and schist) are present. Feldspar fragments are dominated by plagioclase grains (showing mainly Carlsbad+albite polysynthetic twinning), and minor amounts of potassium feldspar grains (as untwined orthoclase) and rare microcline grains (displaying “grid” or “tartan” twinning) are also present. Quartz fragments are dominated by monocrystalline quartz grains, and minor amounts of polycrystalline quartz grains are present. Quartz grains are unaltered, and approximately one-half of the grains have undulose extinction and deformation lamellae, but it is uncertain if these structures were inherited or are secondary in origin. Non-framework grains, accounting for <1% of all grains, include clinopyroxene, orthopyroxene, hornblende, epidote, sphene, and zircon (all relatively unaltered), carbonate allochems (recrystallized fossils, intraclasts, and possibly pellets), siltstone (indented and squished), and biotite and muscovite (bent, frayed, and partly altered to chlorite).

709 The main secondary constituents include calcite, prehnite, chlorite, and illite (all
710 identified optically), as well as kaolinite (identified by XRD). Minor secondary constituents
711 include laumontite, celedonite, pyrite, magnetite, and hematite (all identified optically), in
712 addition to quartz and albite (both identified by XRD). Calcite was observed in all sandstone thin
713 sections. It occurs as specks of microspar replacing plagioclase, and as sparry cement replacing
714 grains and grain interstices (up to 20% of the area in several thin sections). The sparry cement
715 has straight, thick Type II calcite twins and rare curved, thick Type III twins (cf., Weber et al.,
716 2001). Illite was also observed in most thin sections, and it occurs as partial replacements of
717 plagioclase grains, as interstitial material (i.e., the variety 'sericite'), and completely replaces
718 pre-existing grains of undetermined mineralogy (in which illite is relatively coarse-grained and
719 displays bold first-order yellow and red interference colors). Laumontite (*senso stricto*, the
720 mineral is likely leonardite, the partially dehydrated version of laumontite; Neuhoff and Bird,
721 2001) was noted in ~50% of the thin sections. It occurs as clear, irregular masses with distinct
722 cleavage that forms poikilotopic patches replacing grains and as interstitial material. Celedonite
723 was seen in ~25% of the thin sections. It partially replaces pre-existing grains along with
724 chlorite, and completely replaces grains of pre-existing undetermined mineralogy. Celedonite is
725 typically bright blue-green and fibrous, has blue-green and pale green pleochroism, and
726 anomalous brown interference colors. Pyrite and magnetite were found ~75% of the thin
727 sections. They form irregular grains that are widely dispersed throughout the thin sections.
728 Hematite was observed in only a few thin sections and is associated with magnetite. Kaolinite,
729 quartz, and albite, all identified by XRD (< 2 μm size fraction), likely form interstitial material
730 that is too fine-grained to be identified optically. The sandstone thin sections also contain

731 microveins of quartz-prehnite, calcite-prehnite, and calcite-quartz-prehnite, that in turn are cross-
732 cut by calcite microveins.
733 In summary, the dominant secondary mineral assemblage in sandstone is prehnite ±
734 laumontite + chlorite + kaolinite +illite ± celedonite, indicative of high temperature zeolite facies
735 metamorphism (Liou et al., 1987).
736 In addition to the siliciclastic sandstones describe previously, four thin sections from
737 coquina beds ("shell hash") were also examined. The coquinas beds are moderately well sorted
738 bivalve rudstones. Minor amounts of coarse-grained silt to coarse-grained sand, comprising
739 quartz, feldspar and volcanic rock fragments, are present as a matrix. Calcite is abundant and
740 occurs as coarse to very coarse sparry cement displaying straight, thick Type II twins and curved,
741 thick Type III twins. Bivalves have well developed microstyollites, with solution seams
742 highlighted by a film of opaque, black (5Y 2.5/2) material. Several bivalves are also broken and
743 splintered due to compaction. Celedonite is rare and completely replaces pre-existing grains of
744 undetermined mineralogy. Rare magnetite and pyrite occur as widely dispersed irregular grains.
745

746 3.2.2. Mudstone

747 Mudstones are relatively undeformed or have an incipient to moderately developed
748 foliation in thin sections. Undeformed mudstones are moderately to well sorted, and poorly to
749 well laminated with several laminae composed of coarse-grained silt. Rare wispy lamination is
750 present in several thin sections. Mudstones are almost an isotropic, dark grayish brown (10YR
751 4/2) in transmitted light at 35x magnification. Widely dispersed white (10YR 8/1) specks of
752 possibly quartz and plagioclase, and black (5Y 2.5/2) specks of pyrite are also present.

753 The main secondary constituents include quartz, albite, chlorite, and illite (all identified
754 by XRD), and minor amounts of calcite, stipnomelane, actinolite, and pyrite (all identified
755 optically), and rare garnet (identified optically). Quartz, albite, chlorite, and illite, identified by
756 XRD (< 2 μm size fraction), likely form the irresolvable turbid matrix that is too fine grained to
757 identify optically. Calcite is present in most thin sections and forms irregular patches of
758 microspar to sparry cement. Pyrite is rare and occurs as widely dispersed grains and irregular
759 masses.

760 Stipnomelane, actinolite, and garnet are restricted to deformed mudstones. Stipnomelane
761 was observed in ~50% of the thin sections of deformed mudstones. It occurs as small (~0.1 mm
762 long), elongated crystals that are strongly pleochroic dark brown and pale brown, and lack the
763 “bird's eye maple” texture present in biotite. Stipnomelane shows varying degrees of preferred
764 alignment, accounting for the foliation in the deformed mudstones. Actinolite was noted in one
765 thin section and is associated with stipnomelane. Actinolite forms small (~0.2 mm), poorly
766 aligned needles to radiating clusters, is weekly pleochroic pale green to clear, and displays
767 obvious cleavage. Garnet was observed in only two thin sections, and is also associated with
768 stipnomelane. It forms small (~0.3 mm diameter), euhedral grains.

769 In summary, mudstones are characterized by the secondary mineral assemblage quartz +
770 albite + chlorite + illite ± calcite ± stipnomelane that is non-diagnostic for determining the
771 metamorphic facies.

772

773 3.2.3. Hemipelagite

774 Hemipelagites are massive to poorly laminated in thin section. They appear light
775 brownish gray (10YR 6/2) to grayish brown (10YR 5/2) in transmitted light at 35x

magnification. Widely dispersed white (10YR 8/1) specks of quartz and black (5Y 2.5/2) specks and minute cubes of pyrite are also present.

The major secondary constituents include calcite (identified optically), as well as illite, kaolinite, and chlorite (identified by XRD), with minor amounts of celedonite and pyrite (identified optically), and rare rhombohedral 'ghosts' of an unidentified mineral (observed optically). Calcite is ubiquitous and occurs as irregular patches of microspar. Illite, kaolinite, and chlorite, identified by XRD (<2 μm size fraction), likely form the irresolvable turbid matrix that is too fine grained to identify optically. Rare celedonite occurs as distinctive bright blue-green spots that occur widely scattered in the matrix. Small (~ 0.1 mm diameter) rhombohedral "ghosts" observed in the matrix of one thin section may be poorly preserved carbonate (dolomite or siderite), or laumontite crystals. The hemipelagite thin sections also contain microveins of calcite-pyrite.

In summary, hemipelagites are characterized by the secondary mineral assemblage illite + kaolinite + chlorite ± calcite ± celedonite that is also non-diagnostic for determining metamorphic facies.

3.2.4. Volcaniclastics

The volcaniclastic rocks, geochemically classified as dacite-rhyolite (Lowey, 2011), include shard-dominated tuff layers and crystal-dominated tuff layers. The petrology of the crystal tuffs is similar to the siliciclastic sandstones described previously. Vitric tuffs are clast-supported and well sorted. They consist of fine- to medium-grained sand-sized shards that are angular, and platy to cuspate. All of the shards are pseudomorphs of laumontite (viz., leonardite). In addition, some shards appear to have been vesicular, with the vesicles now completely filled

by chlorite. Minor amounts of quartz, plagioclase, volcanic lithic fragments, and rare biotite grains are also present. Vitric tuffs are pale brown (10 YR 6/3) or mottled light gray (10YR 6/1) to very pale brown (10 YR 8/3) in transmitted light at 35x magnification. Most shards have a thin (~0.05 mm) dark grayish brown (10YR 4/2) rim in transmitted light at 35x magnification. When viewed at 500x magnification, the rim consists of minute, subhedral, semi-transparent olive yellow (5Y 6/6) crystals.

The major secondary mineral constituent is laumontite (identified optically and by XRD), with minor amounts of albite, chlorite, illite, prehnite, calcite, pyrite, and palagonite (identified optically), as well as minor amounts of illite, and kaolinite (identified by XRD). Laumontite is ubiquitous in all of the thin sections (~70 % by area). It occurs as clear, irregular masses with distinct cleavage that form poikilotopic patches replacing shards and interstitial material. Albite replaces some plagioclase grains, while other plagioclase grains appear unaltered. Albitized plagioclase appears turbid, particularly towards the center of the grain, and exhibits irregular twin boundaries that reveal a composition of ~Ab_{90}. Pale green chlorite was noted in most of the thin sections. It occurs as specks replacing plagioclase grains, as a partial replacement of biotite grains, as vesicle-filling cement in shards, and likely forms the olive yellow rim on shards. Illite was also observed in all of the thin sections and it occurs as specks replacing plagioclase grains. Calcite was observed in all the thin sections. It occurs as specks of microspar replacing plagioclase grains, and as sparry cement replacing grains and grain interstices. Prehnite was found in ~50 % of the thin sections. It comprises cloudy, granular aggregates that form irregular poikilotopic patches replacing shards and interstitial material. Pyrite is rare and occurs as widely dispersed, irregular grains; and rare spots of brown, semi-translucent material interpreted as palagonite was observed in several thin sections. Quartz, illite, kaolinite, and albite, identified by

XRD (< 2 μm size fraction), likely form interstitial material too fine-grained to be identified optically. Thin sections of vitric tuffs also contain microveins of quartz, calcite, calcite+quartz, laumontite+quartz, and calcite+quartz+laumontite+prehnite.

In summary, vitric tuffs are characterized by the secondary mineral assemblage laumontite ± prehnite + illite + chlorite + quartz, indicative of high temperature zeolite facies metamorphism (Liou et al., 1987).

3.3. X-Ray Diffraction

Results of the XRD analyses are provided in Figure 6 (diffratograms), Figure 7 (compositional pie diagrams), and Supplementary Table S2. XRD analysis of bulk sandstone samples show that they are dominated by plagioclase and quartz. The sandstones contain ~5–9 wt% of material that is <2μm. The clay-size material consists mainly of chlorite, kaolinite, and illite, with minor amounts of calcite, quartz, and plagioclase (Fig. 7). Clay minerals detected in the XRD analysis are difficult to identify by SEM analysis due to a lack of diagnostic morphological features, but EDX analysis corroborates the XRD analysis. The clay minerals occur in the matrix between framework grains (i.e., plagioclase, quartz, calcite, and muscovite) as pore filling material.

XRD analysis of the bulk hemipelagite sample shows that it is dominated by calcite. The hemipelagite contains ~4 wt% of material that is <2μm. The clay-size material consists mainly of chlorite, kaolinite, and illite, with minor amounts of calcite. Clay minerals detected in the XRD analysis are also difficult to identify in by SEM analysis due to a lack of diagnostic morphological features, but EDX analysis corroborates the XRD analysis. Irregular flakes of

illite and poorly formed kaolinite and/or chlorite platelets occur tightly packed between framework grains (i.e., calcite, quartz, and plagioclase).

XRD analysis of the bulk volcaniclastic sample shows that it is dominated by quartz and laumontite. The volcaniclastic contains ~5 wt% of material that is <2μm. The clay-size material consists mainly of laumontite and illite, with minor amounts of kaolinite, chlorite, quartz, albite, and calcite (Fig. 7). SEM analysis reveals a predominance of interlocking aggregates of columnar to tabular structures, and EDX analysis indicates that Si, Al, Ca, and O are the only constituents composing the structures; the morphology and elemental composition of the structures confirm that the structures are laumontite. Clay minerals detected in the XRD analysis are again difficult to identify by SEM analysis due to a lack of diagnostic morphological features, but EDX analysis corroborates the XRD analysis. The abundance of illite indicates the tuff has been altered to a K-bentonite (Huff, 2016).

Only the <2μm material was analyzed in the mudstones. The clay-size material consists mainly of albite, quartz, chlorite, and illite (the two-layer monoclinic polytype $2M_1$), minor amounts of calcite and potassium feldspar, and rare interstratified illite/smectite (I/S) (Fig. 7). In particular, sample GL12-5 displays <10% interstratified I/S characterized by long-range Rietveld ordering (i.e., R3). The KI for mudstone sample GL12-5 is 0.42 $\Delta°2\theta$, and the AI is 0.34 $\Delta°2\theta$, whereas for mudstone sample GL26-1, the KI is 0.26 $\Delta°2\theta$ and the AI is 0.33 $\Delta°2\theta$. Three alteration zones have been defined based on the KI: diagenetic, with KI >0.42 $\Delta°2\theta$; anchizone, with 0.42 $\Delta°2\theta \leq$ KI $\geq$0.25 $\Delta°2\theta$; and epizone, as KI <0.25 $\Delta°2\theta$ (Blenkinsop, 1988; Merriman and Frey, 1999). The anchizone is transitional between diagenesis and metamorphism (i.e., the epizone). The diagenetic zone is subdivided into shallow (KI >1.0 $\Delta°2\theta$) and deep (1.0 $\Delta°2\theta$> KI >0.42 $\Delta°2\theta$) subzones, and the anchizone is subdivided into low (0.42 $\Delta°2\theta$< KI <0.30 $\Delta°2\theta$)

and high subzones (0.30 Δ°2θ< KI <0.25 Δ°2θ) (Valín et al., 2016). Árkai (1991) designated boundaries for the three main KI zones based on AI: diagenetic, with AI >0.33 Δ°2θ; anchizone, with 0.33 Δ°2θ≤ AI ≥0.26 Δ°2θ; and epizone, with AI <0.26 Δ°2θ. Note that KI and AI are defined such that the values decrease with increasing alteration. Mudstone samples from the Dezadeash Formation indicate deep diagenetic to high anchizone conditions.

3.4. Palynomorph Assemblage

Preservation of palynomorphs extracted from the mudstone and hemipelagite samples is very poor (Supplementary Table S3). Only an extremely sparse assemblage of dark brown to black, corroded silhouettes of what appear to be trilete spores, monosulcate pollen grains, and possibly one bisaccate pollen grain are present. The majority of the organic residue is dominated by palynodebris comprising: unstructured amorphous organic matter in the form of small (~20 µm), nearly equidimensional particles that are dark brown to black and semi-opaque or opaque ("black debris"); slightly larger (~50 µm), irregular "fluffy" masses that are dark brown and partly translucent; minor amounts of dark brown globular masses that possibly represent degraded *Botryococcus* colonies; and rare dark brown to black phytoclasts (leaf cuticles?) with no clear internal structure. The spore and pollen "wrecks" indicate a TAI of ~4.5, suggesting mature thermal maturation.

3.5. Conodont Assemblage

Preservation of conodonts obtained from the limestone bolder is excellent (Supplementary Table S4), and includes ramiform elements, *Neogondolella steinbergensis* (Mosher, 1968) and *Epigondolella bidentata* (Mosher 1968) that indicate a Late Triassic (Late

890 Norian) age. Also present are ichthyoliths, microbivalves, and foraminifers. Garcia-Lopez et al.
891 (2001) proposed alteration zones similar to the KI and AI zones: diacaizone, with CAI <4,
892 ancaizone, with 4≥ CAI ≤5.5, and epicaizone, with CAI >5.5, for which the CAI values increase
893 with increasing alteration. The conodonts indicate a CAI of ~4–4.5, suggesting mature thermal
894 maturation and ancaizone conditions.
895
896 ## 3.6. Pyrolysis
897 All but one sample indicates TOC <0.3 wt%, rendering the majority of the T_{max} values as
898 suspect (Supplementary Table S5). Mudstone sample GL4-8 contains 1.26% TOC and has a
899 corresponding T_{max} value of 589 °C. Three stages of thermal maturity with respect to oil source
900 rocks have been designated as follows (Peters and Cassa, 1994): immature, with T_{max} <435 °C
901 and attributed to diagenesis; mature (corresponding to the "oil window"), with T_{max} 435–470 °C
902 and due to catagenesis (increasing pressure and temperature); and postmature, with T_{max} >470 °C
903 and indicative of metagenesis (i.e., incipient metamorphism). The one reliable sample is
904 postmature, suggesting metagenesis conditions. Calculated parameters for this sample indicate
905 HI=5 and OI=33, suggesting Type III (terrestrial) and IV (degraded or inert) kerogen is present.
906 Type III kerogen is also indicated using the values of S2=0.06 and TOC=1.26% from the
907 Dezadeash Formation and the S2 versus TOC graph of Langford and Blanc-Valleron (1990). HI,
908 OI, S2 and TOC parameters are in agreement with the type of organic matter recovered during
909 the processing of samples for palynomorphs.
910 The extremely low TOC values discouraged the use of vitrinite reflectance analysis,
911 perhaps the most widely utilized technique for determining thermal maturity of sedimentary
912 rocks (Allen and Allen, 2013). The percent reflectivity in oil (R_o) of vitrinite (a kerogen maceral)
913 corresponds to the stage of thermal maturity: diagenesis, with R_o <0.5 (also referred to as

914 immature); catagenesis, with >0.5R_o<1.3 (also referred to as mature with >0.5R_o<1.3, and
915 postmature with >1.3 R_o<2); metagenesis, with >2R_o<4 (also referred to as overmature); and
916 values of R_o>4 are in the real of metamorphism (Tissot and Welte, 1984; Hartkopf-Fröder et al.,
917 2015). A correlation between T_{max} and R_o has been proposed by Barker and Pawlewicz (1994)
918 and Jarvie (2018). Barker and Pawlewicz (1994) derived the equation ln(%Rm)=(0.078T_{max})-1.2,
919 which converts the T_{max} of 589 °C obtained from the mudstone sample to 3.8 %Ro. Jarvie (2018)
920 devised the equation Equivalent%R_o=(0.0165T_{max})-6.5143, which converts the mudstone T_{max}
921 value of 589 °C to 3.2 Equivalent%R_o. The T_{max} value of the Dezadeash sample indicates a
922 metagenesis stage of thermal maturation (i.e., overmature), and conversion of the T_{max} value to
923 vitrinite reflectance values is consistent with metagenesis conditions.
924

925 ## 3.7. Subsidence Analysis

926 Parameters used in the subsidence analysis of the Dezadeash Formation are poorly
927 constrained or unknown. Nevertheless, reasonable estimates can be made regarding the life span
928 of the basin, bathymetry of the basin, sediment accumulation rate, and compaction of the basin
929 fill. Based on macrofossils (i.e., *Buchia*), the Dezadeash Formation is Late Jurassic (Oxfordian,
930 163.1 Ma, Ogg et al., 2016) to Early Cretaceous (Valangin, 134.7 Ma, Ogg et al., 2016) in age,
931 equal to a duration of ~30 Ma. This time span is compatible with the life span of rift, forearc,
932 backarc, and foreland basins (Allen and Allen, 2013). Hemipelagite beds consisting of lime
933 mudstone (~30–33% $CaCO_3$) are common in the Dezadeash Formation, indicating that the floor
934 the basin was above the calcite compensation depth (CCD). The CCD at the time of the Jurassic-
935 Cretaceous boundary (145.7 Ma, Ogg et el., 2016) was ~3400–4000 m (van Andel, 1975;
936 Ridgwell, 2004). Furthermore, *Chondrites* and *Zoophycos* occur as endichnial trace fossils within

the hemipelagite beds, whereas *Paleodictyon* and *Urohelminthoida* are present as hypichnial trace fossils on the soles of sandstone beds in thin- to medium-bedded sandstone-mudstone couplets. The two trace fossil assemblages are similar to the *Zoophycos* ichnofacies (intermediate between shelf and bathyal) and *Nereites* ichnofacies (bathyal to abyssal, particularly distal areas of outer fans or fan-fringe facies of lobes and basin plain deposits) of Seilacher (2007), suggesting paleowater depths of 1–4 km. However, ichnofacies are no longer regarded as rigorous indicators of paleobathymetry, and are more reflective of environmental conditions (i.e., substrate and oxygen levels) during deposition (Uchman and Wetzel, 2012). In the absence of unequivocal evidence of the paleobathymetry, a water depth of 1000 m is assumed. In addition, sea-level at the Jurassic-Cretaceous boundary was ~15 m less than the present sea-level (Tennant et al., 2017).

The exposed thickness of the Dezadeash Formation is ~3000 m. This is equivalent to a compacted sediment rate of 100 m/Ma (100 mm/Ka), compatible with sedimentation rates of modern submarine fans (Barnes and Normark, 1985; Reid et al., 1996). The present-day porosity (ϕ_N) for the Dezadeash Formation is estimated to be 0.05 and the porosity when deposited (ϕ_O) is inferred to have been 0.4 (based on porosity of shaly-sand, Sclater and Christie, 1980). The decompacted thickness of the Dezadeash Formation at the time of deposition (T_O), assuming all changes in porosity with depth are the result of compaction (Angevine et al., 1990, their equation 3.1), is ~4750 m. This is equivalent to a decompacted sediment rate of 158 m/Ma (158 mm/Ka) that is also compatible with sedimentation rates of modern submarine fans (Barnes and Normark, 1985; Reid et al., 1996). Taking burial into account and assuming that the base of the Dezadeash Formation was buried to 4000 m (i.e., 3000 m for the Dezadeash Formation plus 1000 m for the Amphitheater Formation), the decompacted thickness of the Dezadeash Formation is ~3700 m.

This is equivalent to a decompacted sediment rate of 123 m/Ma (123 mm/Ka) that is also compatible with sedimentation rates of modern submarine fans (Barnes and Normark, 1985; Reid et al., 1996). The decompacted thicknesses of 4750 m and 3700 m represents a vertical shortening of 36% and 19%, respectively.

The following parameters were used for backstripping the Dezadeash Formation according to a one-dimensional, local isostatic Airy model employing the formula in Angevine et al. (1990, their equation 3.4): decompacted thickness of the basin fill (S*) =3700 m and 4750 m, density of the basin fill sediment (ρ_s) =2685 kg/m^3, density of the asthenosphere (ρ_a)=3300 kg/m^3, density of ocean water (ρ_w)=1028 kg/m^3, water depth of the basin (Wd_i) = 1000 m, and sea-level below present day sea-level (ΔSL_i) =15 m. The calculated tectonic subsidence is ~2000 m and ~2300 m respectively, suggesting that about 50% of the total subsidence is due to tectonic driving forces, and 50% is due to sediment loading of the basin fill. The backstripped depth to the basin basement is equivalent to a tectonic subsidence rate of ~66 m/Ma (66 mm/Ka) and ~76 m/Ma (76 mm/Ka) respectively, compatible with tectonic subsidence rates of forearc and rift basins (Xie and Heller, 2009; Allen and Allen, 2013).

4. Discussion

4.1. Constraints on the burial history of the Nutzotin-Dezadeash basin

Typically, very low-grade metamorphism (VLGM) of siliciclastic sedimentary rocks results in a complex mixture of heterogeneous relic detrital minerals, patchiness of secondary minerals, and variable amounts of altered organic material, all of which may be individually metastable, in addition to an absence of a well developed penetrative tectonic fabric (Kisch, 1991; Merriman and Peacor, 1999). The bulk composition of the sedimentary protolith (i.e.,

983 basically the type of sedimentary rock) exerts a first-order control on the range of secondary
984 minerals formed during VLGM (Caddick and Thompson, 2008; Frey and Kisch, 1987), and
985 therefore a variety of techniques must be employed to determine the post-depositional alteration
986 of rocks of diverse lithologies.

987 The results of various techniques utilized in determining the mineralogic and organic
988 thermal indicators in rocks of diverse lithologies (e.g., sandstone, mudstone, hemipelagite, and
989 tuff) from the Dezadeash Formation are summarized in a correlation diagram (Fig. 8). In
990 particular, secondary mineral assemblages in sandstone and tuff indicate high temperature zeolite
991 facies metamorphism; Kübler indices of illite and Árkai indices of chlorite in mudstone record
992 diagenetic to high anchizone metapelitic conditions; and pyrolysis of organic matter and the
993 color of organic matter (i.e., Thermal Alteration Index of palynomorphs and Conodont Alteration
994 Index) in mudstone and hemipelagite beds suggest that thermal maturation reached catagenesis
995 to mesogenesis stages. Correlation of the various mineralogic and organic thermal indicators is
996 internally consistent and suggests VLGM of the Dezadeash Formation. The development of an
997 incipient slaty cleavage (i.e., S_0-S_1 pencil structure) in the Dezadeash Formation is also
998 compatible with VLGM (Kisch, 1991; Merriman and Peacor, 1999).

999 Note that on the correlation diagram, illite and chlorite crystallinities document slightly
1000 higher thermal alteration than secondary mineral assemblages, whereas organic matter records an
1001 even slightly higher thermal alteration than illite and chlorite crystallinities. This general trend of
1002 increasing thermal alteration from zeolite facies, to diagenesis-anchizone conditions, to
1003 catagenesis-mesogenesis stages is attributed to the various “phases” (i.e., hydrous Ca-Al
1004 silicates, sheet silicates, and organic matter) reacting at different rates, or kinetics. (Kisch, 1987;
1005 Merriman and Frey, 1999; Merriman and Peacor, 1999). The varying reaction kinetics imply that

1006 these out-of-equilibrium phases provide only qualitative estimates of paleopressure and
1007 paleotemperature and (Essene,1989; Frey et al., 1991; Merriman and Peacor, 1999).

1008 A first-approximation of the P-T conditions experienced by the Dezadeash Formation can
1009 be derived from the secondary mineral assemblage: zeolite facies metamorphism is generally
1010 considered to range from 200–300 ˚C with total pressures below 3 kbar (Liou et al., 1987;
1011 Bousquet, et al., 2008), and the high temperature zeolite facies (i.e., laumontite with prehnite) is
1012 calculated to reach a temperature of around 230 ˚C (Liou et al., 1987). In addition, the absence of
1013 wairakite and lawsonite suggests metamorphic conditions are limited by the laumontite-wairakite
1014 and laumontite-lawsonite equilibrium for $P_{tot}=P_{CO2}$, specifically P < 3 kbars and T < 300 °C
1015 (Liou, 1971; Boles and Coombs, 1975). If these P-T values represent the *absolute maximum*
1016 conditions experienced by the Dezadeash Formation, and assuming a rock density of ρ=2685
1017 kg/m^3, the maximum depth of burial of the strata would be ~11 km, equivalent to a maximum
1018 paleogeothermal gradient of ~27 °C/km (i.e., within a "normal" geothermal gradient of 25-30
1019 ˚C/km; Merriman and Frey, 1999). The widespread veining
1020 (quartz±calcite±laumontite±prehnite) in the strata also suggests P-T conditions did not exceed
1021 the brittle-ductile transition zone that occurs at a depth of ~13–18 km and temperatures of ~250–
1022 400 °C (Wikipedia, accessed August 28, 2020).

1023 Other P-T constraints include the laumontite dehydration equilibrium of laumontite=
1024 wairakite+2H_2O at ~230 ˚C and 0.5 kbar, ~255 ±5 ˚C and 1 kbar, and ~282 ±5 ˚C and 2 kbar
1025 (Liou, 1970); the laumontite equilibrium of laumontite=anorthite+2quartz+4H_2O at 310 ±10 ˚C
1026 and 1 kbar, and 317 ±10 ˚C and 2 kbar (Thompson, 1970); the laumontite equilibrium of
1027 laumontite=lawsonite +2quartz+2H_2O at 2.75 ±0.25 kbar and 250 ˚C (Thompson, 1970); the
1028 laumontite stability of paragonite+prehnite+5quartz+6H_2O =2laumontite at <260 ˚C; and the

laumontite stability field restricted to 180-285 ˚C at <3 kbar in the NCASH system (Na_2O-Cao-Al_2O_2-SiO_2-H_2O) with excess H_2O and SiO_2, and the zeolite facies estimated to occur between 210–250 ˚C at 2.1–2.9 kbar (Schmidt et al., 1997).

P-T restrictions from other minerals include the prehnite stability of 3prehnite+chlorite+4quartz+18H_2O=4hulandite+tremolite estimated to be between 200–280 ˚C and <3 kbar (Frey et al., 1991); the prehnite stability calculated at T >200 ˚C and P <2 kbar for low XCO_2 (McSween et al., 2015); clay compositions containing 5-10% smectite in I/S interstratification corresponding to 200–250 ˚C (Weaver, 1989); the R=1 to R=3 transition (i.e., short-range to long-range Rietveld ordering in I/S clay) occurring at ~170–180 ˚C (Aldega et al., 2007); the 1M to 2M polytypism transition in illite between 200–350 ˚C at ~2 kbar (Frey, 1987); straight thick Type II calcite twins developing in the range of 150–300 ˚C (Burkhard, 1993); the diagenesis/anchizone boundary estimated at 240 ±15 ˚C according to fluid inclusion data (Mullis et al., 2017); and the effective closure temperature (i.e., the temperature for 90% track retention) of zircon fission tracks at ~240 ˚C (Bernet and Garver, 2005).

Another estimate of the maximum paleotemperature reach by the Dezadeash Formation can be obtained from the calculated vitrinite reflectance values. Although several empirically based formulas have been derived to translate vitrinite data into peak paleotemperature, the formula by Barker and Pawlewicz (1994), namely T_{peak}=[ln(%R_o) + 1.68]/0.0124, was employed because it is designed for burial heating. Using the calculated equivalent reflectance values of 3.2 and 3.8 for the Dezadeash Formation results in temperatures of 229 ˚C and 243 ˚C, respectively. And based on a diagram of nomograms of vitrinite reflectance vs. time and maximum temperature (Sweeney and Burnham, 1990, their Fig. 5), the same calculated equivalent reflectance values correspond to temperatures between ~220–240 ˚C. Lastly, employing the

Ahrrenius plot of temperature vs. time by Epstein et al., (1977, their Figure 9), the conodont CAI value of 4–4.5 reveals a temperature of ~190–230 ˚C, whereas the same CAI value equates to a maximum temperature of 260–285 ˚C, according to temperatures determined by Raman spectroscopy of carbonaceous material in conodont species (McMillan and Golding, 2019).

Based on the above P-T constraints (particularly the laumontite stability temperature, estimates of the P-T region for the zeolite facies, the diagenesis/anchizone boundary determined from fluid inclusion data, and the effective closure temperature of zircon fission tracks), a reasonable estimate for the maximum P-T conditions experience by the Dezadeash Formation is 2.5 kbar and 250 ˚C. The estimated paleopressure corresponds to a burial depth of 9.5 km (again assuming a rock density of ρ=2685 kg/m^3), equivalent to a maximum paleogeothermal gradient of ~27 °C/km (i.e., still a normal geothermal gradient). The estimated P-T conditions are consistent with the observation by Merriman and Peacor (1999) that burial beneath 4-12 km of overburden are required (assuming a typical geothermal gradient of 25 ˚C/km) to bring about temperatures of 200-300 ˚C that characterize VLGM. Thus, the Nutzotin-Dezadeash basin appears to have been subject to VLGM (the Denali fault did not displace the proximal half of the basin— the Nutzotin Mountains sequence— from the distal half or the Dezadeash Formation until Eocene time), with the Dezadeash Formation reaching the high temperature zeolite facies.

4.2. Implications regarding the tectonic evolution of the Northern Cordillera

The estimated maximum paleotemperature experienced by the Dezadeash Formation, together with published thermochronometric data for the strata, are plotted on a time vs. temperature diagram (Fig. 9). The diagram shows that the Dezadeash Formation underwent rapid, short-term heating followed by gradual, long-term cooling. Also shown in the diagram is

1075 the tectonic subsidence curve calculated for the Dezadeash Formation, indicating rapid, short-
1076 term subsidence followed by gradual, long-term uplift. The general trend of both plots is similar
1077 (i.e., a steep downward slope followed by a gradual upward slope), indicating correspondence
1078 between the diverse types of data.

1079 The thermochronometric data of McDermott et al. (2019) are not plotted in Figure 9
1080 because it is unclear what unit was sampled. On the geologic map of the Kluane Lake area
1081 (Dodds and Campbell, 1992c), their sample is from an area mapped as undifferentiated Upper
1082 Triassic to Lower Cretaceous phyllite, greywacke, and conglomerate that includes presumed
1083 noncalcareous rocks of the McCarthy Formation (Triassic) and rocks of the Dezadeash
1084 Formation (Jurassic-Cretaceous). Perplexingly, McDermott et al. (2019) do not identify any of
1085 the stratigraphic units that their samples are from. Furthermore, the area McDermott et al. (2019)
1086 collected their sample is characterized by intense faulting, and this may have affected the
1087 integrity of their sample, even if it was collected from the Dezadeash Formation. Namely,
1088 McDermott et al. (2019) obtained a ZHe age of ~14 Ma compared to ~60 and ~69 Ma by
1089 Enkelmann et al. (2017), and McDermott et al. (2019) report a ZFT age of is ~136 Ma versus
1090 ~110 Ma by Enkelmann et al. (2017) (Table 1).

1091 Sedimentary basins display different geothermal gradients due to differences in heat flow
1092 associated with various tectonic settings (Siever, 1979; Peacock, 1996; Doglioni et al., 1999;
1093 Woodcock, 2004; Allen and Allen, 2013). Accordingly, the geothermal gradient of a sedimentary
1094 basin may help distinguish the type of basin, and hence the tectonic setting of the basin (Allen
1095 and Allen, 2013). Results of this study suggest the Nutzotin-Dezadeash basin was characterized
1096 by a normal paleogeothermal gradient (~27 ˚C). Forearc, foreland, “failed” rift, and continental
1097 “sag” basins display normal or near normal geothermal gradients (e.g., 20–30 ˚C), whereas

crustal-scale strike-slip, rift and backarc basins are associated with higher geothermal gradients (e.g., 35–50 ˚C) (Siever, 1979; Doglioni et al., 1999; Leloup et al., 1999; Merriman, 2005; Vieira and Hamza, 2018). The secondary clay mineral assemblage observed in the Dezadeash Formation may also be used to infer the tectonic setting of the Nutzotin-Dezadeash basin. According to Merriman (2002, 2005) and Stone and Merriman (2004), clay minerals buried in a sedimentary basin undergo a series of transformations that reflect the geothermal conditions of the basin, as determined by the tectonic setting. Extensional settings, associated with higher than normal paleogeothermal gradients, are characterized by a complex assemblage of both K-rich and Na-rich 2:1 dioctahedral clays (generally aluminous and phengite-poor), whereas convergent settings, associated with lower to normal paleogeothermal gradients, are characterized by a simple assemblage of 2:1 dioctahedral clays (phengitic k-micas, or illite) and rare Na/K-mica (Stone and Merriman, 2004). The secondary clay mineral assemblage observed in the Dezadeash Formation is characterized by a narrow range of clay minerals including $2M_1$ illite and chlorite, suggesting a convergent rather than extensional tectonic setting. Based on the inferred paleogeothermal gradient and secondary clay mineral assemblage of the Dezadeash Formation, rift, backarc, and crustal-scale strike-slip basins fail the "thermal history test".

Sedimentary basins likewise display different tectonic subsidence curves attributed to different tectonic driving mechanisms associated with contrasting tectonic settings (Angevine et al., 1990; Xie and Heller, 2009; Allen and Allen, 2013). Consequently, the tectonic subsidence curve of a sedimentary basin may also help differentiate the type of basin type, and therefore the tectonic setting of the basin (Angevine et al., 1990; Xie and Heller, 2009; Allen and Allen, 2013). The tectonic subsidence curve for the Dezadeash Formation indicates rapid, short-term subsidence of 66–76 m/Ma (66–76 mm/Ka), assuming a basin lifespan of 30 Ma, followed by

gradual, long-term uplift of 22 m/Ma (~22 mm/Ka), assuming uplift lasted about 90 Ma (i.e., from the minimum age of the Dezadeash Formation of 130 Ma, to the maximum age of the Amphitheater Formation of ~40 Ma).

Although several parameters used in backstripping the Dezadeash strata are poorly constrained, these uncertainties tend to affect the absolute value of the calculated tectonic subsidence by ± 100–200 m and not the overall shape of the curve (Gallagher, 1989; Angevine et al., 1990; Audet and McConnell, 1994). Typical tectonic subsidence curves for various basins include: moderately steep to near-vertical linear curves reflecting subsidence rates between 10–100 m/Ma (10–100 mm/Ka) and lifespans of 10–60 Ma for forearc basins; moderately steep linear curves reflecting subsidence rates of 200–400 m/Ma (200–400 mm/Ka) that decrease to 15 m/Ma (15 mm/Ka) and lifespans of 30-70 Ma for backarc basins; upward convex curves reflecting subsidence rates of 200–500 m/Ma (200–500 mm/Ky) and lifespans of 10–50 Ma for peripheral foreland basins; moderately steep linear curves reflecting subsidence rates of <50 m/Ma (<50 mm/Ka) and lifespans of 20–60 Ma for retroarc foreland basins; near-vertical linear curves reflecting subsidence rates of >500 m/Ma (>500 mm/Ka) and lifespans of 3–10 Ma for strike-slip basins; and downward convex curves reflecting subsidence rates of <200 m/Ma (<200 mm/Ka) that decreases exponentially to <50 m/Ma (<50 mm/Ka) and lifespans of 10-100 Ma for rift basins (Angevine and Heller, 1990; Koesoemadinata et al., 1995; Woodcock, 2004; Xie and Heller, 2009; Sinclair and Naylor, 2012; Allen and Allen, 2013). Based on the tectonic subsidence curve calculated for the Dezadeash Formation (i.e., the shape and subsidence rate), together with the inferred life-span of the Nutzotin-Dezadeash basin, peripheral foreland, strike-slip, and rift basins fail the “tectonic subsidence curve test”.

Although tectonic subsidence curves may be a useful tool in basin analysis, they are not a "magic wand" for identifying the tectonic setting of sedimentary basins. The original compilation of tectonic subsidence curves by Xie and Heller (2009) was based on a limited data set, and as they cautioned, the method should be used in parallel with other basin analysis techniques. In addition, some tectonic subsidence curves may represent a complex signal involving multiple tectonic driving mechanisms (Xie and Heller, 2009; Allen and Allen, 2013); tectonic subsidence curves may vary within a basin (Parra et el., 2009; Caravaca et al., 2017); tectonic subsidence curves calculated for basins with a history of overpressuring ignore the evolution of porosity with time (Audet and McConnell, 1994); and tectonic subsidence curves for foreland basins may be influenced by the load of the subducted lithospheric slab (in addition to the topographic load of the thrust wedge) as well as dynamic subsidence due to subduction (Ziegler et al., 2002; Painter and Carrapa, 2013). Despite these caveats, the overall shape of the tectonic subsidence curves generally reflects the main tectonic driving force of the tectonic setting (i.e., downward concave curves corresponding to stretching and thermal cooling of the lithosphere in divergent settings, upward convex curves corresponding to flexural loading of the lithosphere in convergent settings, and near-vertical linear curves corresponding to shearing of the lithosphere in transform settings (Allen and Allen, 2013; Baiyegunhi et al., 2017).

A prevailing model for the tectonic setting of the Nutzotin-Dezadeash basin and Gravina basin invokes deposition in a sinistral transpressional, crustal-scale rift or strike-slip fault between the YCT and WCT (Gehrels et al., 2009; Yokelson et al., 2015; Geisler et al., 2016; Peacha et al., 2016; Beranek et al., 2017). However, the geothermal gradient, time-temperature plot, and tectonic subsidence curve for the Dezadeash Formation are not compatible with a rift or

crustal-scale strike-slip origin. A similar conclusion was reached for the Gravina belt in southeastern Alaska by Stowell et al. (2000).

Current reconstructions of the structural deformation and crustal-scale structure of the northern Cordillera in Yukon suggest that the Dezadeash Formation was thrust to depths >20 km beneath the Blanchard River assemblage, Kluane Schist, and YCT around ~90 Ma (Mezger et al., 2001b; Johnston and Canil, 2007; Stanely, 2012; Vice, 2017). The maximum pressure experienced by the Dezadeash Formation was < 3 kbar and likely ~2.5 kbar (or ~9.5 km of burial), whereas the Blanchard River assemblage experienced 6.3–6.7 kbar (Vice, 2017) or ~23-25 km of burial (assuming a rock density of 2,750 kg/m^3), and the Kluane schist reached 8 kbar or ~30 km of burial (again assuming a rock density of 2,750 kg/m^3) (Stanley, 2012; Vice, 2017). Furthermore, the time vs. temperature graph (Fig. 9) demonstrates that the Dezadeash Formation was undergoing gradual uplift before and during deposition of the Blanchard River assemblage, and that the Dezadeash Formation was also undergoing uplift during the inferred underthrusting of the Blanchard River assemblage and Kluane Schist beneath the YCT. Therefore, the proposed structural deformation and crustal-scale reconstructions are not supported by this study.

Rather, the Dezadeash Formation (and Nutzotin-Dezadeash basin) appears to have been subject to a temporally and spatially separate burial, deformation, and exhumation history than that experienced by the Blanchard River assemblage or Kluane Schist, and was only marginally affected by the Coast Plutonic Complex (Lowey, 2000). Furthermore, the tectono-metamorphic history of the Nutzotin-Dezadeash basin contrasts sharply with that of the Gravina belt and Gravina sequence in southeastern Alaska. The Gravina belt was subject to zeolite to amphibolite facies metamorphism and experienced pressures of 8.7 ± 1 kbar (~25–30 km depth) and temperatures between 465 ± 50 °C to 545 ± 75 °C (McClelland et al., 1991; Cohen and

Lundberg, 1993), whereas the Gravina sequence experienced greenschist to amphibolite facies metamorphism (Rubin and Saleeby, 1992). The tectono-metamorphic history of the Gravina belt and Gravina sequence is attributed to well documented northeast directed underthrusting of both units beneath the WCT in mid-Cretaceous time as a result of final accretion of the WCT to the North American margin (Crawford et al., 1987; Rubin et al., 1990; McClelland et al., 1991; McClelland and Mattinson, 2000; Stowell and Crawford, 2000; Trop and Ridgway, 2007; Trop et al., 2020). The contradistinction in tectono-metamorphic histories of the more northerly Nutzotin-Dezadeash basin compared to the more southerly Gravina basins may be a manifestation the oblique convergence and diachronous, south to north accretion of the WCT and Chitina arc to the YCT (Trop and Ridgway, 2007; Shepard et al., 2013; Sigloch and Mihalynuk, 2017; Trop et al., 2020).

6. Conclusions

Secondary mineral assemblages in sandstone and tuff indicate high temperature zeolite facies metamorphism; Kübler indices of illite and Árkai indices of chlorite in mudstone record diagenetic to high anchizone metapelitic conditions; and pyrolysis of organic matter and the color of organic matter (i.e., Thermal Alteration Index of palynomorphs and Conodont Alteration Index) in mudstone and hemipelagite beds suggest that thermal maturation reached catagenesis to mesogenesis stages. Correlation of the various mineralogic and organic thermal indicators is internally consistent and suggests VLGM of the Dezadeash Formation. The development of an incipient slaty cleavage (i.e., S0-S1 pencil structure) in the Dezadeash Formation is also compatible with VLGM.

Based mainly on published estimates for the laumontite stability temperature, the P-T region for the zeolite facies, the temperature of the diagenesis/anchizone boundary, and the effective closure temperature of zircon fission tracks, a reasonable estimate for the maximum P-T conditions experience by the Dezadeash Formation are 2.5 kbar and 250 ˚C. The estimated paleopressure corresponds to a burial depth of 9.5 km (assuming a rock density of ρ=2685 kg/m^3), equivalent to a maximum paleogeothermal gradient of ~27 °C/km (i.e., a normal geothermal gradient).

The estimated maximum paleotemperature experienced by the Dezadeash Formation, together with published thermochronometric data for the strata, shows that the Dezadeash Formation underwent rapid, short-term heating followed by gradual, long-term cooling. A calculated tectonic subsidence curve for the Dezadeash Formation indicates rapid, short-term subsidence, followed by gradual, long-term uplift. The secondary clay mineral assemblage associated with the rapid heating and subsidence is characterized by a narrow range of clay minerals dominated by $2M_1$ illite and chlorite. The thermal history, subsidence history, and secondary clay mineral assemblage are inconsistent with deposition in peripheral foreland, backarc, strike-slip, and rift basins, in accordance with published geothermal gradients, tectonic subsidence curves, and clay mineral assemblages for different sedimentary basins from various tectonic settings.

The thermal history and subsidence history of the Dezadeash Formation are also inconsistent with reconstructions of the deformation and crustal-scale structure of the Northern Cordillera that posit the Dezadeash Formation was thrust to depths >20 km beneath the Blanchard River assemblage, Kluane Schist, and YCT around ~90 Ma. Rather, the Dezadeash Formation was undergoing cooling and uplift when the Blanchard River assemblage experienced

pressures of 6.3-6.7 kbar (~23-25 km of burial, assuming a rock density of 2,750 kg/m^3), and the Kluane Schist reached pressures of 8 kbar (~30 km of burial, again assuming a rock density of 2,750 kg/m^3) around ~80 Ma. The Dezadeash Formation (and Nutzotin-Dezadeash basin) appears to have experienced a temporally and spatially separate burial, deformation, and exhumation history than that experienced by either the Blanchard River assemblage or Kluane Schist. The tectono-metamorphic history of the Dezadeash Formation contrasts sharply with the Gravina belt and Gravina sequence, which were apparently underthrust (~25-30 km) beneath the YCT.

Acknowledgements

This study was partly funded by the Northern Research Institute and I wish to acknowledge that field work was undertaken in the traditional territory of the Champagne and Aishihik First Nations. Aaron Ogden, Marty Mossop, and Werner Liebau are thanked for providing field assistance in the early phases of this project. Discussions with Stephen Johnston regarding the “Dezadeash molasse” were, as always, entertaining. Data for this research are included in this paper and supplementary information files (available through the Open Science Framework at: https://doi.org/10.17605/OSF.IO/5264J), in addition to data cited from: Enkelmann, E., Piestrzeniewicz, A., Falkowski, S., & Stübner, K., 2017, Thermochronology in southeast Alaska and southwest Yukon: implications for North American plate response to terrane accretion, Earth and Planetary Science Letters, 457, 348–358; and McDermott, R.G., Ault, A.K., Caine, J.S., & Thompson, S.N. , 2019, Thermotectonic history of the Kluane Ranges

and evolution of the eastern Denali fault zone in southwestern Yukon, Canada. Tectonics, 38, 2983–3010. The author declares no conflict of interest.

References

Aldega, L., Corrado, S., Grasso, M., & Maniscalco, R. (2007). Correlation of diagenetic data from organic and inorganic studies in the Appeninic-Maghrebian fold-and-thrust belt: A case study from eastern Sicily. *The Journal of Geology*, 115(3), 335–353. https://doi.org/10.1086/512756

Allen, P.A., & Allen, J.R. (2013). *Basin Analysis: Principles and Application to Petroleum Play Assessment* (3rd Ed.). New York: Wiley-Blackwell.

Amato, J.M., Rioux, M.E., Kelemen, P.B., Gehrels, G.E., Clift, P.D., Pavlis, T.L., & Draut, A.E. (2007), U-Pb geochronology of volcanic rocks from the Jurassic Talkeema Formation and detrital zircons from prearc and postarc sequences: Implications for the age of magmatism and inheritance in the Talkeetna arc. In K.D. Ridgway, J.M. Trop, J.M.G Glen, & J.M. O'Neill (Eds.) T*ectonic Growth of a Collisional Continental Margin: Crustal Evolution of Southern Alaska*, *Geological Society of America Special Paper 431* (pp. 253–271). Boulder, Colorado: Geological Society of America. https://doi.org/10.1130/2007.2431(11)

Anderson, T., Elburg, M.A., & Magwaza, B.N. (2019). Sources of bias in detrital zircon geochronology: Discordance, concealed lead loss and common lead correction. *Earth-Science Reviews*, 197, 1–15. https://doi.org/10.1016/j.earscirev.2019.102899

Anderson, T.H. (2015). Jurassic (170–150 Ma) basins: the tracks of a continental-scale fault, the Mexico-Alaska megashear, from the Gulf of Mexico to Alaska. In T.H. Anderson, A.N. Didenko, C.L. Johnson, A.I. Khanchuk, & J.H. MacDonald, Jr. (Eds.), *Late Jurassic Margin of Laurasia–A Record of Faulting Accommodating Plate Rotation*, *Geological Society of America Special Papers 513* (pp. 1–82). Boulder, Colorado: Geological Society of America. https://doi.org/10.1130/2015.2513(03)

Angevine, C.L., Heller, P.L., & Paola, C. (1990). Quantitative sedimentary basin modeling. *Continuing Education Course Note Series 32*. Tulsa, Oklahoma: The American Association of Petroleum Geologists

Andronicos, C.L., L.S. Hollister, C. Davidson, & D. Chardon (1999). Kinematics and tectonic significance of transpressive structures within the Coast Plutonic Complex, British Columbia. *Journal of Structural Geology*, 21, 229–243. https://doi.org/10.1016/S0191-8141(98)00117-5

Árkai, P. (1991). Chlorite crystallinity: an empirical approach and correlation with illite crystallinity, coal rank and mineral facies as exemplified by Palaeozoic and Mesozoic rocks of northeast Hungary. *Journal of Metamorphic Geology*, 9, 723–734. https://doi.org/10.1111/j.1525-1314.1991.tb00561.x

Armstrong, R.L. (1988). Mesozoic and Early Cenozoic Magmatism of the Canadian Cordillera. *Geological Society of America Special Papers 218*, 55–92. https://doi.org/10.1130/SPE218-p55

Audet, D. M., & McConnell, J. D. C. (1994) Establishing resolution limits for tectonic subsidence curves by forward basin modelling. *Marine Petroleum Geology Letters*, 11, 400–411. https://doi.org/10.1016/0264-8172(94)90058-2

Baiyegunhi, C., Liu, K., & Gwavava, O. (2017) Sedimentation rate and subsidence history of the southeastern Karro basin, South Africa, using 1D backstripping method. *Arabian Journal of Geosciences*, 10(225), 1–21. https://doi.org/10.1007/s12517-07-3009-x

Barker, Ch.E., & Pawlewicz, M.J. (1986). The correlation of vitrinite reflectance with maximum temperature in humic organic matter. In G. Buntebarth & L. Stegena (Eds.), *Lecture Notes in Earth Sciences 5* (pp. 79–93). Paleothermics, Springer-Verlag: Berlin. https://doi.org/10.1007/BFb0012103

Barker, C.E., & Pawlewicz, M.J. (1994). Calculation of vitrinite reflectance from thermal histories and peak temperatures, a comparison of methods. In P. Mukhopadhyay (Ed.), *Vitrinite reflectance as a maturity parameter* (pp. 216–219). ACS Symposium Series, American Chemical Society. https://doi.org/10.1021/bk-1994-0570.ch014

Barker, F. (1987). Cretaceous Chisana island arc of Wrangellia, eastern Alaska. *Geological Society of America Abstracts with Programs*, 19: 580.

Barnes, N.E., & Normark, W.R. (1985). Diagnostic parameters for comparing modern submarine fans and ancient turbidite systems. In: A.H. Bouma, W.R. Normark, and N.E. Barnes (Eds.), *Submarine Fans and Related Turbidite Systems* (pp. 216–219). Springer-Verlag: New York, New York.

Behar, F., Beaumont, V., & Penteado, H.L. (2001). Rock-Eval 6 Technology: Performances and Developments. *Oil & Gas Science and Technology — Rev. IFP*, 56(2), 111–134. https://doi.org/10.2516/ogst:2001013

Beranek, L.P., McClelland, W.C., van Staal, C.R., Israel, S., & Gordee, S.M. (2017). Late Jurassic flare-up of the Coast Mountains arc system, NW Canada, and dynamic linkages across the northern Cordilleran orogen. *Tectonics*, 36, 877–901. https://doi.org/10.1002/2016T004254

Beranek, L. P., C. R. van Staal, S. M. Gordee, W. C. McClelland, S. Israel, & M. G. Mihalynuk (2012). Tectonic significance of Upper Cambrian-Middle Ordovician mafic volcanic rocks on the Alexander terrane, Saint Elias Mountains, northwestern Canada. *Journal of Geology*, 120, 293–314. https://doi.org/10.1086/664788

Beranek, L.P., van Staal, C.R., McClelland, W.C., Joyce, N., & Israel, S. (2014). Late Paleozoic assembly of the Alexander-Wrangellia-Peninsular composite terrane, Canadian and Alaskan Cordillera. *Geological Society of America Bulletin*, 126, 1531–1550. https://doi.org/ doi:10.1130/31066.1

Berg, H.C., Jones, D.L., & Richter, D.H. (1972). Gravina-Nutzotin belt — tectonic significance of an Upper Mesozoic sedimentary and volcanic sequence in southern and southeastern Alaska (pp. D1–D24). *United States Geological Survey, Professional Paper 800D*.

Bernet, M., & Garver, J.I. (2005). Fission-track analysis of detrital zircon. *Reviews in Mineralogy and Geochemistry*, 58, 205–238. https://doi.org/10.2138/rmg.2005.58.8

Bird, K.J., Burruss, R.C., & Pawlewicz, M.J. (1999). Thermal maturity, Chapter VR. In *The oil and gas resource potential of the 1002 area, Arctic National Wildlife Refuge, Alaska*. ANWR Assessment Team, *United States Geological Survey, Open File Report 98-34*.

Blatt, H. (1992). *Sedimentary Petrology* (2nd Ed.). W H Freeman & Co.: San Francisco.

Blenkinsop, T.G. (1988). Definition of low-grade metamorphic zones using illite crystallinity. *Journal of Metamorphic Geology*, 6, 623–636. https://doi.org/10.1111/j.1525-1314.1988.tboo444.x

Boggs, S., Jr. (2009). *Petrology of sedimentary rocks* (2nd Ed.). Cambridge University Press, Cambridge, UK.

Boles, J.R., & Coombs, D.S. (1975). Mineral reactions in zeolite Triassic tuff, Hokonui Hills, New Zealand. *Geological Society of America Bulletin*, 86, 163–173. https://doi.org/10.1130/0016-7606(1975)86<163:MRIZTT>2.0.CO;2

Bond, G.C., & Kominz, M.A. (1984). Construction of tectonic subsidence curves for the early Paleozoic miogeocline, southern Canadian Rocky Mountains: Implications for subsidence mechanisms, age of breakup, and crustal thinning. *Geological Society of America Bulletin*, 95, 155–173. https://doi.org/10.1130/0016-7606(1984)95%3C155:COTSCF%3E2.0.CO;2

Bousquet, R., Oberhänsli, R., Goffé, B., Wiederkehr, M., Koller, F., Schmid, S.M., Schuster, R., Engi, M., Berger, A., & Martinotti, G. (2008). Metamorphism of metasediments at the scale of an orogen: a key to the Tertiary geodynamic evolution of the Alps. In S. Siegesmund, B. Fugenschuh & N. Froitzheim (Eds.), *Tectonic aspects of the Alpine-Dinarde-Carpathian system* (pp.393–411). *Geological Society, London, Special Publications, 298*. https://doi.org/10.1144/SP298.18

Brew, D.A., & A.B. Ford (1983). Comment on "Tectonic accretion and the origin of the two major metamorphic and plutonic welts in the Canadian Cordillera". *Geology*, 11, 427–428.

Brew, D.A., & Ford, A.B., (1998), The Coast Mountains structural zones in southeastern Alaska; descriptions, relations, and lithotectonic terrane significance. In J.E. Gray, J.E. & J.R. Riehle (Eds.), *Geologic studies in Alaska by the United States Geological Survey, 1996* (pp. 183–192). *United States Geological Survey, Professional Paper 1595*.

Brew, D.A., & Morrell, R.P. (1983). Intrusive rocks and plutonic belts in southeastern Alaska, U.S.A. In J.A. Roddick (Ed.), *Circum-Pacific plutonic terranes* (pp. 171–193). *Geological Society of America, Memoir 159*. Geological Society of America.

Burkhard, M. (1993). Calcite twins, their geometry, appearance and significance as stress-strain markers and indicators of tectonic regime: a review. *Journal of Structural Geology*, 15 (3-5), 351–368. https://doi.org/10.1016/0191-8141(93)90132-T

Caddick, M.J., & Thompson A.B. (2008). Quantifying the tectono-metamorphic evolution of peletic rocks from a wide range of tectonic settings: mineral compositions in equilibrium. *Contributions to mineralogy and Petrology*, 156, 177–195. https://doi.org//10.1007/s00410-008-0280-6

Canil, D., Johnston, S.T., D'Souza, R.J., & Heaman, L.M. (2015). Protolith of ultramafic rocks in the Kluane Schist, Yukon, and implications for arc collisions in the norther Cordillera. *Canadian Journal of Earth Sciences*, 52, 431–443. https://doi.org/10.1139/cjes-2014-0138

Caravaca, G., Brayard, A., Vennin, E., Guiraud, M., Le Pourhiet, L., Grosjean, A.-S., Escaguel, G., Bylundi, K.G., Jenks, J.F., and Stephen, D.A. (2017). Controlling factors for differential subsidence in the Sonoma Foreland basin (Early Triassic, western USA). *Geological Magazine*, 155(6), 1305–1329. https://doi.org/10.1017/S0016756817000164

Chardon, D., Andronicos, C.L., & L.S. Hollister (1999). Large-scale shear zone patterns and displacements within magmatic arcs: The Coast Plutonic Complex, British Columbia. *Tectonics*, 18, 278–292. https://doi.org/10.1029/1998TC900035

Chen, Y., Gu, Y.J., Currie, C.A., Johnston, S.T., Hung, S.-H., Schaffer, A.J., & Audet, P. (2019). Seismic evidence for a mantle suture and implications for the origin of the Canadian Cordillera. *Nature Communications*, 1–8. https://doi.org/10.1038/s41467-019-09084-8

Clague, J.J. (1979). The Denali fault system in southwest Yukon Territory — A geologic hazard? In *Current research part A* (pp. 169–178). *Geological Survey of Canada, Paper 79-1A*

Clift, P.D., Draut, A.E., Kelemen, P.B., Blusztajn, J., & Greene, A. (2005). Stratigraphic and geochemical evolution of an oceanic arc upper crustal section: the Jurassic Talkeetna Volcanic Formation, south-central Alaska. *Geological Society of America Bulletin*, 117, 902–925. https://doi.org/10.1130/B25638.1

Cohen, H.A. (1992). *Stratigraphic, sedimentologic, and provenance constraints on the evolution of the Gravina belt, northern southeast Alaska* (Doctoral dissertation). Princeton, New Jersey: Princeton University.

Cohen, H.A., Hall, C.M., & Lundberg, N. (1995). 40Ar/39Ar dating of detrital grains constrains the provenance and stratigraphy of the Gravina belt, southeastern Alaska. *Journal of Geology*, 103, 327–337. https://doi.org/10.1086/629750

Cohen, H.A., & Lundberg, N. (1993). Detrital record of the Gravina arc, southeastern Alaska: petrology and provenance of Seymour Canal Formation sandstones. *Geological Society of America Bulletin*, 105: 1400–1414. https://doi.org/10.1130/ 0016-7606(1993)1052.3.CO;2

Crawford, M.L., Hollister, L.S., & Woodsworth, G.J. (1987). Crustal deformation and regional metamorphism across a terrane boundary, Coast Plutonic complex, British Columbia. *Tectonics*, 6(3), 343–361. https://doi.org/10.1029/TC006i003p00343

Dalrymple, R.W., 2010. Interpreting Sedimentary Successions: Facies, Facies Analysis and Facies Models. In N.P. James & R.W. Dalrymple (Eds.), *Facies models 4* (pp. 3–18). *Geological Association of Canada*. St John's, Newfoundland: Geological Association of Canada.

Dickinson, W.R., Beard, L.S., Brakenridge, G.R., Erjavec, J.L., Ferguson, R.C., Inman, K.F., et al. (1983). Provenance of North American Phanerozoic sandstones in relation to tectonic setting.

Geological Society of America Bulletin, 94, 222–235. https://doi.org/10.1130/0016-7606(1983)942.0.CO;2

Dickinson, W.R., & Suczek, C.A. (1979). Plate tectonics and sandstone compositions. *American Association of Petroleum Geologists Bulletin*, 63, 2164–2182. https://doi.org/10.1306/2F9188FB-16CE-11D7-8645000102C1865D

Dodds, C.J., & R.B. Campbell (1988). Potassium-argon ages of mainly intrusive rocks in the Saint Elias Mountains, Yukon and British Columbia. *Geological Survey Canada, Paper 87-16.*

Dodds, C.J., & Campbell, R.B. (1992a). Overview, legend and mineral deposit tabulations for Geology of southwest Kluane Lake map area (115G and F[E1/2]), Yukon Territory, Open File 2188; Geology of Mount St. Elias map area (115B and C[E1/2]), Yukon Territory, Open File 2189; Geology of southwest Dezadeash map area (115A), Yukon Territory, Open File 2190; and Geology of northeast Yakutat Map Area (114O) and Tatshenshini River (114 P) map areas. *Geological Survey of Canada, Open File 2191*.

Dodds, C.J., & Campbell, R.B. (1992b). Geology, SW Dezadeash map area [115A], Yukon Territory. *Geological Survey of Canada, Open File 2190*. https://doi.org/10.4095/133476

Dodds, C.J., & Campbell, R.B. (1992c). Geology, SW Kluane Lake map area [115G & F[E 1/2]], Yukon Territory. *Geological Survey of Canada, Open File 2188.* https://doi.org/10.4095/133474

Doglioni, C., Harabaglia, P., Merlini, S., Mongelli, F., Peccerillo, A. & Piromallo, C. (1999): Orogens and slabs vs their direct of subduction. *Earth Science Reviews*, 45, 167–208. https://doi.org/10.1016/S0012-8252(98)00045-2

Dusel-Bacon, C., Csejtey, B., Jr., & Foster, H.L. (1993). Distribution, facies, ages, and proposed tectonic associations of regionally metamorphosed rocks in east- and south-central Alaska. *United States Geological Survey, Professional Paper 1497-C*. https://pubs.er.usgs.gov/publication/pp1497C

Eisbacher, G.H. (1976). Sedimentology of the Dezadeash flysch and its implications for strike-slip faulting along the Denali fault, Yukon Territory and Alaska. *Canadian Journal of Earth Sciences*, 13, 1495–1513. https://doi.org/10.1139/e76-157

Eisbacher G.H. (1985). Pericollisional strike-slip faults and synorogenic basins, Canadian Cordillera. In K.T. Biddie and N. Christie-Blick (Eds.), *Strike-Slip Deformation, Basin Formation, and Sedimentation* (pp. 265–282). *Special Publication of the Society of Economic Paleontologists and Mineralogists 37*.

Enkelmann, E., Piestrzeniewicz, A., Falkowski, S., & Stübner, K. (2017). Thermochronology in southeast Alaska and southwest Yukon: implications for North American plate response to terrane accretion. *Earth and Planetary Science Letters*, *457*, 348–358. https://doi.org/10.1016/j.epsl.2016.10.032

Epstein, A.G., Epstein, J.B., & Harris, L.D. (1977). Conodont Color Alteration Index to Organic Metamorphism. *United States Geological Survey, Professional Paper 995*.

Essene, E.J. (1989). The current status of thermometry in metamorphic rocks. In J.S. Daly, R.A. Cliff, & B.W.D. Yardley (Eds.), Evolution of metamorphic belts (pp. 1–44). *Geological Society of America Special Publication 43*.

Falkowski, S., & Enkelmann, E. (2016). Upper-crustal cooling of the Wrangellia composite terrane in the northern St. Elias Mountains, western Canada. *Lithosphere*, 8(4), 359–378. https://doi.org/10.1130/L508.1

Frey, M. (1987). Very low-grade metamorphism of clastic sedimentary rocks. In M. Frey (Ed.), *Low temperature metamorphism* (pp. 9–58). Blackie & Sons Ltd.: Bishopbriggs, Glasgow.

Frey, M., de Capitani, C., & Liou, J.G. (1991). A new petrogenetic grid for low-grade metabasites. *Journal of Metamorphic Geology, 9,* 497–509. https://doi.org/10.1111/j.1525-1314.1991.tb00542.x

Frey, M., & Kisch. HJ. (1987). Scope of subject. In M. Frey (Ed.), *Low temperature metamorphism* (pp. 1-8). Blackie and Son Ltd.: Bishopbriggs, Glasgow.

Fu, R.R., Kent, D.V., Hemming, S.R., Gutierrez, P., & Creveling, J.R. (2020). Testing the occurrence of Late Jurassic true polar wander using the La Negra volcanics of northern Chile. *Earth and Planetary Science Letters*, 529, 1–10. https://doi.org/10.1016/j.epsl.2019.115835

Gallagher, K. (1989). An examination of some uncertainties associated with estimates of sedimentation rates and tectonic subsidence. *Basin Research*, 2(93), 97–114. https://doi.org/10.1111/j.1365-2117.1989.tb00029.x

García-López, S., Bastida, F., Aller., J., & and Sanz-López, J. (2001). Geothermal palaeogradients and metamorphic zonation rom the conodont colour alteration index (CAI). *Terra Nova*, 13, 79–83. https://doi.org/10.1046/j.1365-3121.2001.00328.x

Gehrels, G.E. (2000). Reconnaissance geology and U-Pb geochronology of the western flank of the Coast Mountains between Juneau and Skagway, southeastern Alaska. In H.H. Stowell & W.C. McClelland (Eds.), *Tectonics of the Coast Mountains, Southeastern Alaska and British Columbia, Geological Society of America Special Paper 343* (pp. 213–233). Boulder, Colorado: Geological Society of America. https://doi.org/10.1130/0-8137-2343-4.213

Gehrels, G.E., & Berg, H.C. (1994). Geology of southeastern Alaska. In G. Plafker, & H.C. Berg (Eds.), *The Geology of Alaska* (pp. 451–576). *Geological Society of America*, *Vol. G-1*. Boulder, Colorado: The Geology of North America. https://doi.org/10.1130/DNAG-GNA-G1.451

Gehrels, G.E., McClelland, W.C., & Yokelson, I. (2017). Reply to "Comment on U-Pb and Hf isotope analysis of detrital zircons from Mesozoic strata of the Gravina belt, southeast Alaska" by Yokelson et al. (2015). *Tectonics*, *36*, 2741–2743. https://doi.org/10.1002/2017TC004735

Gehrels, G.E., Rusmore, M., Woodsworth, G., Crawford, M., Andronicos, C., Hollister, L., et al. (2009).U–Th–Pb geochronology of the Coast Mountains batholith in north coastal British Columbia: Constraints on age and tectonic evolution. *Geological Society of America Bulletin*, 121, 1341–1361. https://doi.org/10.1130/B26404.1

Geisler, D., Gehrels, Pech, M., White, C., Yokelson, I. G.E., & McClelland (2016). Canadian *Journal of Earth Sciences*, 53, 979–992. https://doi.org/10.1139/cjes-2015-0240

Greene, A.R., Scoates, J.S., Weis, D., Katvala, E.C., Israel, C., & Nixon, G.T. (2010). The architecture of oceanic plateaus revealed by the volcanic stratigraphy of the accreted Wrangellia oceanic plateau. *Geosphere*, 6, 47–73. https://doi.org/10.1130/ GES00212.1

Hampton, B.A., Ridgway, K.D., & Gehrels, G.E. (2010). A detrital record of Mesozoic island arc accretion and exhumation in the North American Cordillera: U–Pb geochronology of the Kahiltna basin, southern Alaska. *Tectonics*, 29, 1–21. https://doi.org/10.1029/2009TC002544

Hancock, P.L. (1982). Distinction between cleavage and joint using fracture separation. In G.J. Borradaille, M.B. Baly, & C. McA. Powell (Eds.), *Atlas of deformational and metamorphic rock fabrics* (pp.186–187). Springer-Verlag: New York, New York.

Haeussler, P.J. (1992). Structural evolution of an arc-basin: the Gravina belt in central southeastern Alaska. *Tectonics*, 11(6), 1245–1265. https://doi.org/10.1029/92TC01107

Harris, A.G., & Sweet, W.C. (1989). Mechanical and chemical techniques for separating microfossils from rock, sediment and residue matrix. In R.M. Feldmann, R.E. Chapman, and J.T. Hannibal (Eds.), *Paleotechniques* (pp. 70–86). *Paleontological Society Special Publication 4*. Bethesda, Maryland: Paleontological Society. https://doi.org/10.1017/S2475262200005013

Hartkopf-Fröder, C., Königshof, P., Littke, R., & Schwarzbauer, J. (2015). Optical thermal maturity parameters and organic geochemical alteration at low grade diagenesis to anchimetamorphism: A review. *International journal of Coal Geology*, 150-151, 74–119. https://doi.org/10.1016/j.coal.2015.06.005

Héroux, Y., Chagnon, A., & Bertrand, R. (1979). Compilation and correlation of major maturation indicators. *American Association of Petroleum Geologists Bulletin, 63*, 12, 2128–2144.

Hietpas, J., Samson, S.D., & Moecher, D.P. (2010). Recovering tectonic events from the sedimentary record: Detrital monazite plays in high fidelity. *Geology*, 38(2), 167–170.

https://doi.org/10.1130/G30265.1

Hildebrand, R.S. (2013). Mesozoic assembly of the North American Cordillera. *Geological Society of America Special Paper 495*. Boulder, Colorado: Geological Society of America. https://doi.org/10. 1130/SPE495

Himmelberg, G.R., Brew, D.A., & Ford, A.B. (1995). Low-grade M1 metamorphism of the Douglas Island Volcanics, western metamorphic belt near Juneau. In P. Schiffman & H.W. Day (Eds.), Low-grade metamorphism of mafic rocks (pp. 51–66). *Geological Society of America, Special Paper 296*. Boulder, Colorado: Geological Society of America. https://doi.org/10.1130/SPE296-p51

Hudson, T. L. (1983) Calc-alkaline plutonism along the Pacific rim of southern Alaska. In J.A. Roddick (Ed.). Circum-Pacific Plutonic Terranes (pp. 159–169). *Geological Society of America, Memoir 159*.

Huff, W.D. (2016). K-bentonites: A review. *American Mineralogist*, 101,43–70. https://doi.org/10.2138/am-2016-5339

Ibañez-Mejia, M., Pullen, A., Pepper, M., Urbani., F., Ghoshal, G., & Ibañez-Mejia, J.C. (2018). Use and abuse of detrital zircon U-Pb geochronology— A case from the Río Orinoco delta, eastern Venezuela. *Geology*, 46, 1–4. https://doi.org/10.1130/G45596.1

Ingram, G. M., & Hutton, D. H. W. (1994). The Great Tonalite Sill: Emplacement into a contractional shear zone and implications for Late Cretaceous to early Eocene tectonics in southeastern Alaska and British Columbia. *Bulletin of the Geological Society of America*, 106, 715–728.

Jarvie, D. (2018). Correlation of Tmax and measured vitrinite reflectance. Accessed August 18, 2019. https://www.wildcattechnologies.com/application/files/9915/1689/1979/Dan_Jarvie_Correlation_of_Tmax_and_measured_vitrinite_reflectance.pdf

Johnston, S.T., & Canil, D. (2007). Crustal structure of SW Yukon, northern Cordillera: implications for crustal growth in a convergent margin orogen. *Tectonics*, 26, 1–18. https://doi.org/10.1029/206TC001950

Kisch, H.J. (1987). Correlation between indicators of very low-grade metamorphism. In M. Frey (Ed.), *Low temperature metamorphism* (pp. 227-300). Blackie & Sons Ltd.: Bishopbriggs, Glasgow.

Kisch, H.J. (1991). Illite crystallinity: recommendations on sample preparation, X-ray diffraction settings, and interlaboratory samples. *Journal of Metamorphic Geology*, 9(6), 665–670. https://doi.org/10.1111/j.1525-1314.1991.tb00556.x

Klepeis, K.A., M.L. Crawford, & G. Gehrels (1998). Structural history of the crustal-scale Coast shear zone north of Portland, southeast Alaska and British Columbia. *Journal of Structural Geology,* 20, 883–904. https://doi.org/10.1016/S0191-8141(98)00020-0

Koesoemadinata, R.P., Samuel, L., & Tachjudin, M.I. (1995). Subsidence curves and modelling of some Indonesian Tertiary basins. *Geological Society of Malaysia Bulletin* 37, 205–230. https://doi.org/10.1306/A25FE711-171B-11D7-8645000102C1865D

Kozinski, J. (1985). *Sedimentology and tectonic significance of the Nutzotin mountains sequence, Alaska* (Master's thesis). Albany, New York: State University of New York.

Lafargue, E., Marquis, F., & Pillot, D. (1998) Rock-Eval 6 applications in hydrocarbon exploration, production, and soil contamination studies. *Oil & gas Science and technology — Rev. IFP*, 53(4), 421–437. https://doi.org/10.2516/ogst:1998036

Langford, F.F., & Blanc-Valleron, M. -M. (1990). Interpreting rock-eval pyrolysis data using graphs of pyrolizable hydrocarbons vs. total organic carbon. *American Association of Petroleum Geologists Bulletin, 74*(6), 799–804. https://doi.org/10.1306/0C9B238F-1710-11D7-8645000102C1865D

Lanthram, E.H., Pomeroy, J.S., Berg, H.C., & Loney, R.A. (1965). Reconnaissance Geology of Admiralty Island Alaska. *United States Geological Survey, Bulletin 1181-R.*

Leloup, P.H., Ricard, Y., Battaglia, J., & Lacassin, R. (1999). Shear heating in continental strike-slip shear zones: Model and field examples. *Geophysical Journal International*, 136, 19–40. https://doi.org/10.1046/j.1365-246X.1999.00683.x

Liou, J.G., (1970). Synthesis and stability relations of wairakite, $CaAl_2Si_4O_{12}{\cdot}2H_2O$. *Contributions to Mineralogy and Petrology*, 27, 259–282. https://doi.org/10.1007/BF00389814

Liou, J.G. (1971). Synthesis and stability relations of prehnite, $Ca_2Al_2Si3_3O_{10}(OH)_2$. *The American Mineralogist*, 56, 507–531.

Liou, J.G., Maruyama, S., & Cho, M. (1987). Very low-grade metamorphism of volcanic and volcaniclastic rocks- mineral assemblages and mineral facies. In M. Frey (Ed.), *Low temperature metamorphism* (pp. 59–113). Blackie & Sons Ltd.: Bishopbriggs, Glasgow.

Lowey, G.W. (1980). *Depositional themes in a turbidite succession, Dezadeash Formation (Jura–Cretaceous), Yukon* (Master's thesis). Calgary, Alberta: University of Calgary.

Lowey, G.W. (1992). Variation in bed thickness in a turbidite succession, Dezadeash Formation (Jurassic–Cretaceous), Yukon, Canada: Evidence of thinning-upward and thickening-upward cycles. *Sedimentary Geology*, 78, 217–232. https://doi.org/10.1016/0037-0738(92)90021-I

Lowey, G.W. (1998). A new estimate of the amount of displacement on the Denali Fault system based on the occurrence of carbonate megaboulders in the Dezadeash Formation (Jura-

Cretaceous), Yukon, and the Nutzotin Mountains sequence (Jura–Cretaceous), Alaska. *Bulletin of Canadian Petroleum Geology*, 46, 379–386. https://doi.org/10.35767/gscpgbull.46.3.379

Lowey, G.W. (2000). The Tatshenshini shear zone (new) in southwestern Yukon, Canada: Comparison with the Coast shear zone in British Columbia and southeastern Alaska and implications regarding the Shakwak suture. *Tectonics*, 19(3), 512–528. https://doi.org/10.1029/1999TC001119

Lowey, G.W. (2007). Lithofacies analysis of the Dezadeash Formation (Jura– Cretaceous), Yukon, Canada: The depositional architecture of a mud/sand-rich turbidite system. *Sedimentary Geology*, 198, 273–291. https://doi.org/10.1016/j. sedgeo.2006.12.011

Lowey, G.W. (2011). Volcaniclastic gravity flow deposits in the Dezadeash Formation (Jura–Cretaceous), Yukon, Canada: Implications regarding the tectonomagmatic evolution of the Chitina arc in the northern Cordillera of North America. *Lithos*, 125, 86–100. https://doi.org/10.1016/j.lithos.2011.01.014

Lowey, G.W. (2017). Comment on "U-Pb and Hf isotope analysis of detrital zircons from Mesozoic strata of the Gravina belt, southeast Alaska" by Yokelson et al. (2015). *Tectonics, 36*, 2736–2740. https://doi.org/10.1002/2017TC004507

Lowey, G.W. (2019). Provenance analysis of the Dezadeash Formation (Jurassic–Cretaceous), Yukon, Canada: Implications regarding a linkage between the Wrangellia composite terrane and the western margin of Laurasia. *Canadian Journal of Earth Science*s, 56(1), 77–10.

https://doi.org/10.1139/cjes-2017-0244

MacKevet, E.M., Jr. (1971). Stratigraphy and general geology of the McCathy C-5 Quadrangle, Alaska. *United States Geological Survey, Bulletin 1323*. https://pubs.usgs.gov/bul/1323/report.pdf

MacKevett, E.M., Jr. (1978). Geologic map of the McCarthy Quadrangle, Alaska. *United States Geological Survey, Map I-1032*. Scale 1:250,000. https://doi.org/10.3133/i1032

Manselle, P., Brueseke, M.E., Trop, J.M., Benowitz, J.A., Snyder, D.C., & Hart, W.K. (2020). Geochemical and stratigraphic analysis of the Chisana Formation, Wrangellia terrane, eastern Alaska: insights into Early Cretaceous magmatism and tectonism along the northern Cordilleran margin. *Tectonics*, 39(8), e2020TC006131. https://doi.org/10.1029/2020TC006131

Manuszak, J.D. (2000). *Sedimentary and structural record of late Jurassic–early Cretaceous collisional tectonics, Nutzotin and Mentasta Mountains, east-central Alaska* (Master's thesis). West Lafyette, Indiana: Purdue University.

Manuszak, J.D., & Ridgway, K.D. (2000). Stratigraphic architecture of the Upper Jurassic–Lower Cretaceous Nutzotin Mountains sequence, Nutzotin and Mentasta Mountains, Alaska. In *Short Notes on Alaska Geology 1999* (pp. 63–75). *Alaska Division of Geological and Geophysical Surveys, Professional Report 119.*

Manuszak, J.D., Ridgway, K.D., Trop, J.M., & Gehrels, G.E. (2007). Sedimentary record of the tectonic growth of a collisional continental margin: Upper Jurassic-Lower Cretaceous Nutzotin Mountains sequence, eastern Alaska Range, Alaska. In K.D. Ridgway, J.M. Trop, J.M.G Glen and J.M. O'Neill (Eds.), *Tectonic growth of a collisional continental margin: Crustal evolution of southern Alaska* (pp. 345–377). *Geological Society of America Special Paper 431*. Boulder, Colorado: Geological Society of America. https://doi.org/10.1130/2007.2431(14)

McClelland, W.C., Anovitz, L.M., & Gehrels, G. 1991. Thermobarometric constraints on the structural evolution of the Coast Mountains batholith, central southeastern Alaska. *Canadian Journal of Earth Sciences*, 28, 912–928. https://doi.org/10.1139/e91-083

McClelland, W.C., Gehrels, G.E., and Saleeby, J.B. (1992a). Upper Jurassic-Lower Cretaceous basinal strata along the Cordilleran margin: implications for the accretionary history of the Alexander-Wrangellia-Peninsular terrane. *Tectonics*, 11: 823–835. https://doi.org/10.1029/92TC00241

McClelland, W.C., Gehrels, G.E., Samson, S.D., & Patchett, P.J. (1992b). Protolith relations of the Gravina Belt and Yukon–Tanana terrane in central southeastern Alaska. J*ournal of Geology*, 100, 107–123.

McClelland, W.C., Gehrels, G.E., Scott D. Samson, S.D., & Patchett, P.J. (1991). Protolith Relations of the Gravina Belt and Yukon-Tanana Terrane in Central Southeastern Alaska. *Journal of Geology*,100, 107–123. https://www.jstor.org/stable/30082321

McClelland, W. C., & Mattinson, J. M. (2000), Cretaceous-Tertiary evolution of the western Coast Mountains, central southeastern Alaska. In H.H. Stowell & W.C. McClelland (Eds.), *Tectonics of the Coast Mountains, Southeastern Alaska and British Columbia* (pp. 159–182). *Geological Society of America Special Paper 343*. Boulder, Colorado: Geological Society of America. https://doi.org/10.1130/0-8137-2343-4.159

McDermott, R.G., Ault, A.K., Caine, J.S., & Thompson, S.N. (2019). Thermotectonic history of the Kluane ranges and evolution of the eastern Denali fault zone in southwestern Yukon, Canada. *Tectonics*, 38, 2983–3010. https://doi.org/10.1029/2019TC005545

McMillan, R., & Golding, M. (2019). Thermal maturity of carbonaceous material in conodonts and the Color Alteration Index: independently identifying maximum temperature with Raman spectroscopy. *Palaeogeography, Palaeoclimatology, Palaeoecology*, 534, 1–11. https://doi.org/10.1016/j.palaeo.2019.109290

McSween, H.Y., Labotka, T.C., & Viviano-Beck, C.E. (2015). Metamorphism in the Martian crust. *Meteoritics & Planetary Scienc*e 50, Nr 4, 590–603. https://doi.org/10.1111/maps.12330

Merriman, R.J. (2002). Contrasting clay mineral assemblages in British Lower Paleozoic slate belts: The influence of geotectonic setting. *Clay Minerals*, 37, 207–219. http://doi.org/10.1180/0009855023720041

Merriman, R.J. (2005). Clay minerals and sedimentary basin history. *European Journal of Mineralogy,* 17, 7–20. https://doi.org/10.1127/0935-1221/2005/0017-0007

Merriman, R.J., & Frey, M. (1999). Patterns of very low-grade metamorphism in metapelitic rocks. In M. Frey, & D. Robinson (Eds.), *Low-grade metamorphism* (pp. 61–107). Blackwell Science Ltd.: Osney Mead, Oxford. https://doi.org/10.1002/9781444313345.ch3

Merriman, R.J., & Peacor, D.R. (1999). Very low-grade metapelites: mineralogy, microfabrics and measuring reaction progress. In M. Frey, & D. Robinson (Eds.), *Low-grade metamorphism* (pp. 10–60). Blackwell Science Ltd.: Osney Mead, Oxford. https://doi.org/10.1002/9781444313345.ch2

Meunier, A., Velde, B., & Zalba, P. (2004). Illite K–Ar dating and crystal growth processes in diagenetic environments: A critical review. *Terra Nova*, 16, 296–304. https://doi.org/10.1111/j.1365-3121.2004.00563.x

Mezger, J.E. (1997). *Tectonometamorphic evolution of the Kluane metamorphic assemblage, SW Yukon: Evidence for Late Cretaceous eastward subduction of oceanic crest underneath North America* (Doctoral dissertation). Edmonton, Alberta: University of Alberta.

Mezger, J.E., Chacko, T., & Erdmer, P. (2001a). Metamorphism at a late Mesozoic accretionary margin: a study from the Coast Belt of the North American Cordillera. *Journal of Metamorphic Geology*, 19, 121–137. https://doi.org/10.1046/j.0263-4929.2000.00300.x

Mezger, J.E., Creaser, R.A., Erdmer, P., & Johnston, S.T. (2001b). A Cretaceous back-arc basin in the Coast Belt of the northern Canadian Cordillera: Evidence from geochemical and neodymium isotope characteristics of the Kluane metamorphic assemblage, southwest Yukon. *Canadian Journal of Earth Sciences*, 38, 91–103. https://doi.org/10.1139/e00-076

Miller, T.P., 1994. Pre-Cenozoic plutonic rocks in mainland Alaska. In: G. Plafker & H.C. Berg, (Eds.), *The Geology of Alaska* (pp. 535–554). *Geological Society of America*, *Geology of North America, Vol. G-1*. Geological Society of America.

Moecher, D.P., & Sampson, S.D. (2006). Differential zircon fertility of source terranes and natural bias in the detrital zircon record: Implications for sedimentary provenance analysis. *Earth and Planetary Science Letters*, 247(3), 252–266. https://doi.org/10.1016/j.epsl.2006.04.035

Monger, J.W.H. (2014). Logan medallist 1. Seeking the suture: The Coast–Cascade conundrum. *Geoscience Canada*, 41, 379–398. https://doi.org/10.12789/geocanj.2014.41. 058

Monger, J.W.H., & Journeay, J.M. (1994). Guide to the geology and tectonic evolution of the southern Coast Mountains. *Geological Survey of Canada*, *Open File 2490*.

Monger, J.W.H., & Nokleberg, W.J. (1996), Evolution of the northern North American Cordillera: Generation, fragmentation, displacement and accretion of successive North American

plate-margin arcs. In A.R. Coyner & P.L. Fahey (Eds.), *Geology and Ore Deposits of the American Cordillera* (pp. 1133–1152). *Geological Society of Nevada, Symposium Proceedings Vol. III*.

Monger, J.W.H., & Price, R. (2002). The Canadian Cordillera: Geology and tectonic evolution. *CSEG Recorder*, 17, 18–36.

Monger, J.W.H., Price, R.A., & Tempelman-Kluit, D.J. (1982). Tectonic accretion and the origin of the two major metamorphic and plutonic welts in the Canadian Cordillera. *Geology*, 10, 70–75. https://doi.org/10.1130/0091-7613(1982)102.0.CO;2

Monger, J.W.H., van der Heyden, P., Journeay, J.M., Evenchick, C.A., & Mahoney, J.B. (1994). Jurassic–Cretaceous basins along the Canadian Coast Belt: Their bearing on pre-mid-Cretaceous sinistral displacements. *Geology*, 22, 175–178. https://doi.org/10.1130/0091-7613(1994)0222.3.CO;2

Moore, J.C. and Connelly, W. (1979). Tectonic history of the continental margin of southwestern Alaska, Late Triassic to earliest Tertiary. In A. Sisson (Ed.), *The Relationship of Plate Tectonics to Alaskan Geology and Resources* (pp. H1-H29). Alaska Geological Society: Anchorage, Alaska.

Mullis, J., Mählmann, R.F., & Wolf, M. (2017). Fluid inclusion microthermometry to calibrate vitrinite reflectance (between 50 and 270 °C), illite Kübler-index data and the

diagenesis/anchizone boundary in the external part of the Central Alps. *Applied Clay Science*, 143, 307–319. https://doi.org/10.1016/j.clay.2017.03.023

Munsell Color (1994). *Munsell Soil Color Charts* (Revised Edition). Windsor, New York: Macbeth Division of Kollmogen Instruments Corporation.

Nelson, J.L., Colpron, M., & Israel, D. (2013). The cordillera of British Columbia, Yukon, and Alaska: tectonics and metallogeny. In N. Colpron, T. Bissig, B.G. Rusk, & J.F.H. Thompson (Eds.), *Tectonics, metallogeny, and discovery: The North American cordillera and similar accretionary settings (*pp. 53–110). *Special Publications of the Society of Economic Geologists, Vol. 17*. Society of Economic Geologists: Littleton, Colorado. https://doi.org/10.5382/SP.17.03

Neuhoff, P.S., & Bird, D.K. (2001). Partial dehydration of laumontite: Thermodynamic constraints and petrogenetic implications. *Mineralogical Magazine*, 65(1), 59–70. https://doi.org/10.1180/002646101550127

Nokleberg, W.J., Jones, D.L., & Silberling, N.J. (1985). Origin and tectonic evolution of the Maclaren and Wrangellia terranes, eastern Alaska Range, Alaska. *Geological Society of America Bulletin*, 96, 1251–1270. https://doi.org/10.1130/0016- 7606(1985)962.0.CO;2

Nokleberg, W.J., Parfenov, W.J., Monger, J.W.H., Norton, I.O., Khanchuk, A.I., Stone, D.B., Scotese, C.R., Scholl, D.W., & Fujita, K. (2000). Phanerozoic Tectonic Evolution of the Circum-North Pacific. *United States Geological Survey, Professional Paper 1626*.

Nokleberg, W.J., Plafker, G., & Wilson, F.H. (1994). Geology of south-central Alaska. In G. Plafker, & H.C. Berg (Ed.), *The Geology of Alaska* (pp. 311–366). *Geological Society of America, Geology of North America, Vol. G-1*. Geological Society of America: Boulder, Colorado. https://doi.org/10.1130/DNAG-GNA-G1.311

Ogg, J.G., Ogg, G., & F. M. Gradstein, F.M. (2016). *A Concise Geologic Time Scale: 2016*. Elsevier: New York. New York.

Orchard, M.J., & Forster, P.J.L. (1991). Conodont color and thermal maturity of the Late Triassic Kunga Group, Queen Charlotte Islands, British Columbia. In *Evolution and hydrocarbon potential of the Queen Charlotte Basin, British Columbia* (pp. 453–464). *Geological Survey of Canada, Paper 90-10*. https://doi.org/10.4095/131983

Painter, C.S., & Carrapa, B. (2013). Flexure versus dynamic processes of subsidence in the North American Cordillera foreland basin. *Geophysical Research Letters*, 40, 4242–4253. https://doi.org/10.1002/grl.50831

Parra, M., Jaramillo, C., Strecker, M.R., Sobel, E.R., Quiroz, L., Rueda, M., & Torres, V. (2009). Orogenic wedge advance in the northern Andes: Evidence from the Oligocene-Miocene sedimentary record of the medina basin, eastern Cordillera, Columbia. *Geological Society of America Bulletin*, 121(5/6), 780–800. https://doi.org/10.1130/B26257.1

Passchier, C.W., & Trouw, R.A.J. 1996. *Micro-tectonics*. Springer-Verlag: New York, New York.

Pavlis, T.L., Amato, J.M., Trop, J.M., Ridgway, K.D., Roeske, S.M., & Gehrels, G.E. (2019). Subduction polarity in ancient arcs: a call to integrate geology and geophysics to decipher the Mesozoic tectonic history of the Northern Cordillera of North America. *Geological Society of America Today, 29*. https://doi.org/10.1130/GSATG3402A.1

Pavlis, T.L., & Roeske, S.M. (2007). The Border Ranges fault system, southern Alaska, In K.D. Ridgway, J.M. Trop, J.M.G. Glen, & J.M. O'Neill (Eds.), *Tectonic growth of a collisional continental margin: Crustal evolution of Southern Alaska* (pp. 95–127). *Geological Society of America Special Paper 431*. Boulder, Colorado: Geological Society of America. https://doi.org/10.1130/2007.2431(05)

Peacock, S.M. (1996). Thermal and petrologic structure of subduction zones. In G.E. Bebout, D.W. Scholl, S.H. Kirby & J.P. Platt, (Eds.), *Subduction top to bottom*, *Geophysical Monograph 96* (pp. 119-133). https://doi.org/10.1029/GM096p0119

Pecha, M.E., Gehrels, G.E., McClelland, W.C., Giesler, D., White, C., & Yokelson, I. (2016). Detrital zircon U-Pb geochronology and Hf isotope geochemistry of the Yukon-Tanana terrane, Coast Mountains, southeast Alaska. *Geosphere*, 12(5), 1556–1574. https://doi.org/10.1130/GES01301.1

Peters, K.E., (1986). Guidelines for evaluating petroleum source rock using programmed pyrolysis. *American Association of Petroleum Geologists Bulletin*, 70, 318–329. https://doi.org/10.1306/94885688-1704-11D7-8645000102C1865D

Peters, K. E. and Casa, M. R. (1994) Applied source rock geochemistry. In L. B. Magoon and W. G. Dow (Eds.), The Petroleum System from Source to Trap, *The American Association of Petroleum Geologists, Memoir* 60, pp. 93–120. https://doi.org/10.1306/M60585C5

Plafker, G., & Berg, H.C. (1994). Overview of the geology and tectonic evolution of Alaska. In G. Plafker & H.C. Berg (Eds.), *The Geology of Alaska* (pp. 989–1021). *Geology of North America, Vol. G-1*. Boulder, Colorado: Geological Society of America. https://doi.org/10.1130/DNAG-GNA-G1.989

Plafker, G., Moore, J. C., & G. R. Winkler (1994), Geology of the southern Alaska margin. In G. Plafker & H.C. Berg, (Eds.), *The Geology of Alaska* (pp. 389–449). *Geology of North America, Vol. G-1*. Boulder, Colorado: Geological Society of America.

Plafker, G., Nokleberg, W.J., & Lull, J.S. (1989). Bedrock geology and tectonic evolution of the Wrangellia, Peninsular, and Chugach terranes along the trans-Alaska crustal transect in the Chugach Mountains and southern Copper River basin, Alaska. *Journal of Geophysical Research: Solid Earth*, 94, 4255–4295. https://doi.org/10.1029/JB094iB04p04255

Randive, K.R., K. R. Hari, K.R., M. L. Dora, M.L., Malpe, D.B. & Bhondwe, A.A. (2014).

Study of Fluid Inclusions: Methods, Techniques and Applications. *Gondwana Geological Magazine*, 29(1-2), 19–28. https://www.researchgate.net/publication/275337661_Study_of_Fluid_Inclusions_Methods_Techniques_and_Applications

Reading, H.G. (1980). *Sedimentary environments and facies*. Oxford Blackwell Scientific Publications.

Reed, B.L., Miesch, A.T., & Lanphere, M.A. (1983). Plutonic rocks of Jurassic age in the Alaska–Aleutian Range batholith: Chemical variations and polarity. *Geological Society of America Bulletin*, 94, 1232–1240. https://doi.org/10.1130/0016-7606(1983)94<1232:PROJAI>2.0.CO;2

Reid, R.P., Carey, S.N., & Ross, D.R. (1996). Late Quaternary sedimentation in the Lesser Antilles island arc. *Geological Society of America Bulletin*, 108, 78–100. https://doi.org/10.1130/0016-7606(1996)108<0078:LQSITL>2.3.CO;2

Reiners, P.W., & Ehlers, T. (2005). Low-Temperature Thermochronology: Techniques, Interpretations, and Application. *Reviews in mineralogy and geochemistry 58*. Mineralogical Society of America. https://doi.org/10.1515/9781501509575

Richter, D.L. (1976). Geologic map of the Nabesna Quadrangle, Alaska. *United States Geological Survey, Miscellaneous Investigations Series Map I-932*. 1:250,000 scale.

Ridgway, K.D., Sweet, A.R., & Cameron, A.R. (1995). Climatically induced floristic changes across the Eocene-Oligocene transition in the northern high latitudes, Yukon Territory, Canada. *Geological Society of America Bulletin*, 107(6), 676–696. https://doi.org/10.1130/0016-7606(1995)107%3C0676:CIFCAT%3E2.3.CO;2

Ridgway, K.D., Trop, J.M., Nokleberg, W.J., Davidson, C.M., & Eastham, K.R. (2002). Mesozoic and Cenozoic tectonics of the eastern and central Alaska range: Progressive basin development and deformation in a suture zone. *Geological Society of America Bulletin*, 114(12), 1480–1504. https://doi.org/10.1130/0016-7606(2002)114%3C1480:MACTOT%3E2.0.CO;2

Ridgwell, A. (2004). A Mid Cenozoic revolution in the regulation of ocean chemistry. *Marine Geology*, 217, 339–357. https:/doi.org/10.1016/j.margeo.2004.10.036

Rioux, M., Hacker, B., Mattinson, J., Kelemen, P., Hanghoj, K., & Plank, T. (2003). The role of intermediate to felsic plutonism in the accreted Talkeetna arc, south-central Alaska. *Geological Society of America, Abstracts with Programs*, 35, 430.

Rioux, M., Hacker, B., Mattinson, J., Kelemen, P., Blusztajn, J., & Gehrels, G. (2007). Magmatic development of an intra-oceanic arc: high-precision U–Pb zircon and whole-rock isotopic analyses from the accreted Talkeetna arc, south-central Alaska. *Geological Society of America Bulletin*, 119, 1168–1184. https://doi.org/10.1130/B25964.1

Roeske, S.M., Pavlis, T.L., Snee, L.W., & Sisson, V.B. (1991). 40Ar/39Ar isotopic ages from the combined Wrangellia-Alexander terrane along the Border Ranges fault system in the eastern Gugach Mountains and Glacier Bay, Alaska. In *Geologic Studies in Alaska by the United States Geological Survey 1990* (pp. 180–195).

Roeske, S.M., Snee, L.W., & Pavlis, T.L. (2003). Dextral-slip reactivation of an arc-forearc boundary during Late Cretaceous–Early Eocene oblique convergence in the northern Cordillera. In V.D. Sisson, M. Roeske & T.L. Pavlis (Eds.), *Geology of a transpressional orogen developed during ridge–trench interaction along the North Pacific margin* (pp. 141–170). *Geological Society of America Special Papers, Vol. 371*. Boulder, Colorado: Geological Society of America. https://doi.org/10.1130/0-8137-2371-X.141

Rubin, C.M., & Saleeby, J.B. (1991). The Gravina Sequence: remnants of a Mid-Mesozoic Oceanic Arc in Southern Southeast Alaska. *Journal of Geophysical Research*, 96, 14,551–14,568. https://doi.org/10.1029/91JB00591

Rubin, C.M., & Saleeby, J.B. (1992) Tectonic history of the eastern edge of the Alexander terrane, Southeast Alaska. *Tectonics*, 11(3), 586–602. https://doi.org/10.1029/91TC02182

Rubin, C.M., Saleeby, J.B., Cowan, D.S., Brandon, M.T., & McGroder, M.F. (1990). Regionally extensive mid-Cretaceous west-vergent thrust system in the northwestern Cordillera: implications for continent-margin tectonism. *Geology*, 18, 276–280. https://doi.org/10.1130/0091-7613(1990)018%3C0276:REMCWV%3E2.3.CO;2

Saleeby, (1983). Accretionary tectonics of the North American Cordillera. *Annual Review of Earth and Planetary Sciences*, 15, 45–73. https://doi.org/10.1146/annurev.ea.11.050183.000401

Schmidt, D., Schmidt, S.Th., Mullis, J., Mählmann, R.F. & Frey, M. (1997). Very low-grade metamorphism of the Taveyanne formation of western Switzerland. *Contributions to Mineralogy and Petrology, 129,* 385–403. https://doi.org/10.1007/s004100050344

Sclater, J.G., & Christie, P.A.F. (1980). Continental stretching: an explanation of the post-mid-Cretaceous subsidence of the central North Sea basin. *Journal of Geophysical Research*, 85, 3711-3739. https://doi.org/10.1029/JB085iB07p03711

Seilacher, A. (2007). *Trace fossil analysis*. Springer: New York, New York.

Shepard, G.E., Müller, R.D., & Seton, M. (2013). The tectonic evolution of the Arctic since Pangea breakup: Integrating constraints from surface geology and geophysics with mantle structure. *Earth-Science Reviews*, 124, 148–183. https://doi.org/10.1016/j.earscirev.2013.05.012

Short, E.J., Snyder, D.C., Trop, J.M., Hart, W.K., & Layer, P.W. (2005). New findings on Early Cretaceous volcanism within the allochthonous Wrangellia terrane, south-central Alaska: Stratigraphic, geochronologic, and geochemical data from the Chisana Formation, Nutzotin Mountains. *Geological Society of America, Abstracts with Programs*, 37, 81.

Siever, R. (1979). Plate-tectonic controls on diagenesis. *The Journal of Geology*, 87, 127–155. https://www.jstor.org/stable/30060249

Sigloch, K., & Mihalynuk, M.G. (2017). Mantle and geological evidence for a Late Jurassic-Cretaceous suture spanning North America. *Geological Society of America Bulletin,* 129(11/12), 1489–1520. https://doi.org/10.1130/B31529.1

Sinclair, H.D., & Naylor, M. (2012). Foreland basin subsidence driven by topographic growth versus plate subduction. *Geological Society of America Bulletin*, 124(3/4), 368–379. https://doi.org/10.1130/B30383.1

Stamatakos, J.A., Trop, J.M., & Ridgway, K.D. (2001). Late Cretaceous paleogeography of Wrangellia: Paleomagnetism of the MacColl Ridge Formation, southern Alaska, revisited. *Geology*, 29, 947–950. https://doi.org/10.1130/0091-7613(2001)029<0947:LCPOWP>2.0.CO;2

Stanley, B. (2012). *Structural geology and geochronology of the Kluane Schist, southwest Yukon Territory* (Master's thesis). Waterloo, Ontario: University of Waterloo. http://hdl.handle.net/10012/7096

Staplin, F. L. (1969). Sedimentary organic matter, organic metamorphism, and oil and gas occurrence. *Bulletin of Canadian Petroleum Geologists*, 17, 47–66. https://doi.org/10.35767/gscpgbull.17.1.047

Stone, P., & Merriman, R.J. (2004). Basin history favours an accretionary origin for the Southern Uplands terrane, Scottish Caledonides. *Journal of the Geological Society*, London, 161, 829–836. https://doi.org/10.1144/0016-764903-170

Stowell, R. R., & Crawford, M. L., (2000). Metamorphic history of the Coast Mountains orogen, western British Columbia and southeastern Alaska. In H.H. Stowell & W.C. McClelland (Eds.), *Tectonics of the Coast Mountains, Southeastern Alaska and British Columbia* (pp. 257–283). *Geological Society of America Special Paper 343*. Boulder, Colorado: Geological Society of America. https://doi.org/10.1130/0-8137-2343-4.257

Stowell, H.H., & R.J. Hooper (1990). Structural development of the western metamorphic belt adjacent to the Coast Plutonic Complex: Evidence from Holkham Bay. *Tectonics*, 9, 391–407. https://doi.org/10.1029/TC009i003p00391

Stowell, H.H., Green, N.L. & Hooper, R.J., (2000). Geochemistry and tectonic setting of basaltic volcanism, northern Coast Mountains. In H.H. Stowell & W.C. McClelland (Eds.), *Tectonics of the Coast Mountains, Southeastern Alaska and British Columbia* (pp. 235–255). *Geological Society of America Special Paper 343*. Boulder, Colorado: Geological Society of America. https://doi.org/10.1130/0-8137-2343-4.235

Sturrock, D.L. (1975). *The Pyroxenite Creek ultramafic complex: an Alaska-type ultramafic intrusion in southwest Yukon* (Master's thesis). Vancouver, British Columbia: University of British Columbia.

Sturrock, D.L., Armstrong, R.L., & Maxwell, R.B. (1980). Age and Sr isotope composition of the Pyroxenite Creek ultramafic complex, southwestern Yukon Territory: An Alaskan-type ultramafic intrusion. In *Current Research, Part B* (pp. 185–188), *Geological Survey of Canada Paper 80-1B*.

Sweeney, J.J., & Burnham, A.K. (1990). Evaluation of a simple model of vitrinite reflectance based on chemical kinetics. *The American Association of Petroleum Geologists Bulletin*, 74, 1559–1570. https://doi.org/10.1306/0C9B251F-1710-11D7-8645000102C1865D

Tempelman-Kluit, D.J. (1976). The Yukon Crystalline terrane: Enigma in the Canadian Cordillera. *Geological Society of America Bulletin 87*, 1343–1357. https://doi.org/10.1130/0016-7606(1976)87<1343:TYCTEI>2.0.CO;2

Tennant, J.P., Mannion, P.D., Upchurch, P., Sutton M.D., & Price, G.D. (2017). Biotic and environmental dynamics through the Late Jurassic-Early Cretaceous transition: Evidence for protracted faunal and ecological turnover. *Biological Reviews*, 92, 776–814. https://doi.org/10.31233/osf.io/gnsb7

Thompson, A.B. (1970). Laumontite equilibria and the zeolite facies. *American Journal of Science*, 269, 267–275. https://doi.org//10.2475/ajs.269.3.267

Tissot, B.P., & Welte, D.H (1984). *Petroleum Formation and Occurrence* (2nd Ed.). Springer-Verlag: Berlin, Germany.

Traverse, A. (1988). *Paleopalynology*. Unwin Hyman: New York, New York.

Trop, J.M, Benowitz, J.A., Koepp, D.O., Sunderlin, D., Brueske, M.E., Layer, P.W., & Fitzgerald, P.G. (2020). Stitch the ditch: Nutzotin Mountains (Alaska) fluvial strata and a dike record ca. 117-114 Ma accretion of Wrangellia with western North America and initiation of the Totschunda fault. *Geosphere*, 16(1), 82–110. https://doi.org/10.1130/GES02127.1

Trop, J.M., & Ridgway, K.D. (2007). Mesozoic and Cenozoic tectonic growth of southern Alaska: a sedimentary basin perspective. In K.D. Ridgway, J.M. Trop & J.M. O'Neils (Eds.), *Tectonic growth of a collisional continental margin; crustal evolution of southern Alaska* (pp. 55–94). *Geological Society of America Special Paper 421*. The Geological Society of America. https://doi.org/10.1130/2007.2431(04)

Trop, J.M., Ridgway, K.D., Manuszak, J.D., & Layer, P. (2002). Mesozoic sedimentary-basin development on the allochthonous Wrangellia composite terrane, Wrangell Mountains basin, Alaska: A long-term record of terrane migration and arc construction. *Geological Society of America Bulletin*, 114, 693–717. https://doi.org/10.1130/0016-7606(2002)1142.0.CO;2

Uchman, A. and Wetzel, A. (2012). Deep-sea fans (Chapter 21, 643–671). In R.G. Bromley & D. Knaust (Eds.), *Trace Fossils as Indicators of Sedimentary Environments*. Developments in Sedimentology 64. Elsevier: Amsterdam. https://doi.org/10.1016/B978-0-444-53813-0.00021-6

van Andel, T.H. (1975). Mesozoic/Cenozoic compensation depth and the global distribution of calcareous sediments. *Earth and Planetary Science Letters*, 26, 187–194. https://doi.org/10.1016/0012-821X(75)90086-2

van der Heyden, P. (1992). A Middle Jurassic to Early Tertiary Andean-Sierran arc model for the Coast Belt of British Columbia. *Tectonics*, 11, 82–97. https://doi.org/10.1029/ 91TC02183

van Hite, J.E. (1978). Geohistory analysis- application of micropaleontology in exploration geology. *American Association of Petroleum Geologists Bulletin*, 62, 201–222. https://doi.org/10.1306/C1EA4815-16C9-11D7-8645000102C1865D

Vice, L. (2017). *Late Cretaceous to Paleocene evolution of the Blanchard River assemblage, southwest Yukon: implications for Mesozoic accretionary processes in the northwestern Cordillera* (Master's thesis). Burnaby, British Columbia: Simon Fraser University

Vieira, F., & Hamza, V. (2018). Global heat flow: New estimates using digital maps and GIS techniques. *International Journal of Terrestrial Heat Flow and Applied Geothermics*, 1(1), 6–13. https://doi.org/10.31214/ijthfa.v1i1.6

Weaver, C.E. (1989). *Clays, Muds and Shales*. Developments in Sedimentology 44, Elsevier: Amsterdam.

Weber, J.C., Ferrill, D.A., & Roden-Tice, M.K. (2001). Calcite and quartz microstructural geothermometry of low-grade metasedimentary rocks, Northern Range, Trinidad. *Journal of Structural Geology*, 23(1), 93–112. https://doi.org/10.1016/S0191-8141(00)00066-3

Wheeler, J.O., & McFeely, P. (1991). Tectonic assemblage map of the Canadian Cordillera and adjacent parts of the United States of America. *Geological Survey of Canada, Map 1712A*. Scale 1:2,000,000. https://doi.org/10.4095/133549

Wikipedia, 2020. "*Brittle-ductile transition zone*". Accessed August 29, 2020. https://en.wikipedia.org/wiki/Brittle%E2%80%93ductile_transition_zone

Wolf, K.H., & Chilingarian, G.V. (1976). Diagenesis of sandstones and compaction. In G.V. Chilingarian & K.H. Wolf (Eds.), *Developments in sedimentology, Volume 18B* (pp. 69–444). *Compaction of coarse-grained sediments II*. Elsevier Scientific Publishing Company: New York, New York. https://doi.org/10.1016/S0070-4571(08)71100-2

Woodcock, N.H. (2004). Life span and fate of basins. *Geology*, 32(8), 685–688. https://doi.org/10.1130/G20598.1

Xie, X., & Heller, P.L. (2009). Plate tectonics and basin subsidence history. *Geological Society of America Bulletin*, 121(1/2), 55–64. https://doi.org/10.1130/B30383.1

Yokelson, I., Gehrels, G.E., Pecha, M., Giesler, D., White, C., & McClelland, W.C. (2015). U–Pb and Hf isotope analysis of detrital zircons from Mesozoic strata of the Gravina belt, southeast Alaska. *Tectonics*, 34, 2052–2066. https://doi.org/10.1002/ 2015TC003955

Zhang, W. Johnston, S.T. & Currie, C.A. (2019). Kimberlite magmatism induced by west-dipping subduction of the North American plate. *Geology, 47*, 395–398. https://doi.org/10.1130/G45813.1

Ziegler, P.A., Bertotti, G., & Cloetingh, S. (2002). Dynamic processes controlling foreland development — the role of mechanical (de)coupling of orogenic wedges and forelands. *European Geoscience Union Stephan Mueller Special Publication Series, 1* (pp. 17–56). https://doi.org/10.5194/smsps-1-17-2002

Table 1. Published low-temperature thermochronometric data, Dezadeash Formation, Yukon, Canada.

Sample	Lithology	Elevation (m)	AHe (Ma)	ZHe (Ma)	AFT (Ma)	ZFT (Ma)
KLB04	metapelite	605	17.8 ± 1.6	59.7 ± 8.1	n.a.	n.a.
KLB91	mudstone	725	11.4 ± 0.8	68.8 ± 2.3	n.a.	109.9 ± 8.9
61115-2A	metagreywacke	941	n.a.	14.0 ± 0.4	n.a.	136.5 ± 8.5
T_c (ºC)			70	180	120	240
PRZ (ºC)			40-70	130-180	n.a.	n.a.
PAZ (ºC)			n.a.	n.a.	60-120	180-240

•AHe= apatite (U-Th)/He, ZHe= zircon (U-Th)/He, AFT= apatite fission-track, and ZFT= zircon fission-track thermochronometer age.
•T_c= closure temperature (radioactive decay product retained below this temperature, but not above it; also the temperature of a mineral at the time given by its radiometric age).
•PRZ= partial retention zone (temperature window over which radioactive decay product is retained).
•PAZ= partial annealing zone (temperature window over which radioactive decay product is preserved). Temperatures from Brandon and Vance (1998) and Peyton and Carrapa (2013). Note that the temperatures are only approximate because they depend on the cooling rate, chemistry of the mineral, and grain-size of the mineral (Brandon and Vance, 1998).
•Samples KLB4 and KLB91 from Enkelmann et al. (2017). Sample 61115-2A from McDermott et al. (2019), although it is uncertain if this came from the Dezadeash Formation.

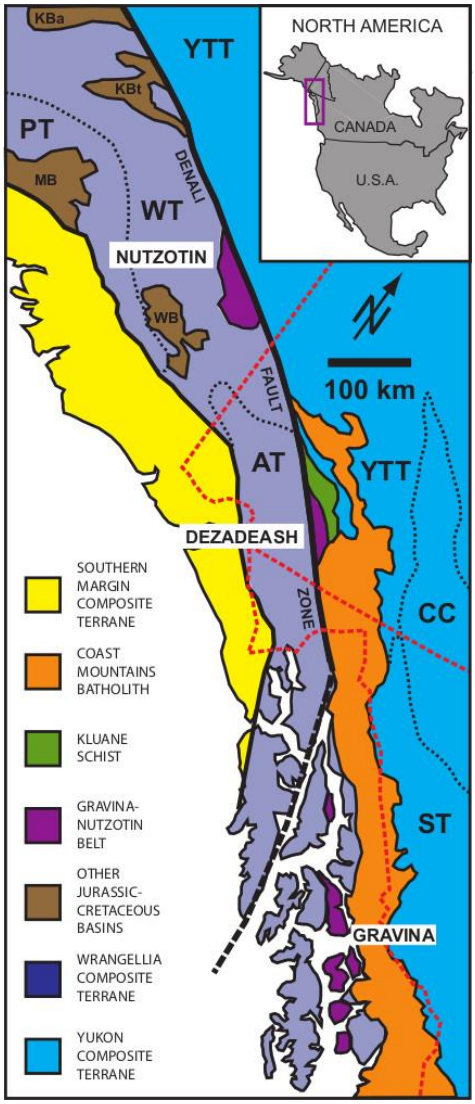

Fig. 1. Location map and geologic setting of the Dezadeash Formation, Yukon (compiled from MacKevett 1978; Wheeler and McFeely 1991; and Monger 2014). AT, Alexander terrane; CC, Cache Creek terrane; PT, Peninsular terrane; ST, Stikine terrane; Y, Yakutat terrane; YTT, Yukon-Tanana terrane; WT, Wrangellia terrane. Kootenay, Cassiar, and Quesnel terranes not shown. Other Jurassic-Cretaceous basins not part of the Gravina-Nutzotin belt: KBa, Kahiltna basin-Alaska Range; KBt, Kahiltna basin-Talkeetna Mountains; MB, Matanuska Valley basin; WB, Wrangell Mountains basin; T, Talkeetna arc; C, Chitina arc; A, Chisana arc; K, Kluane arc.

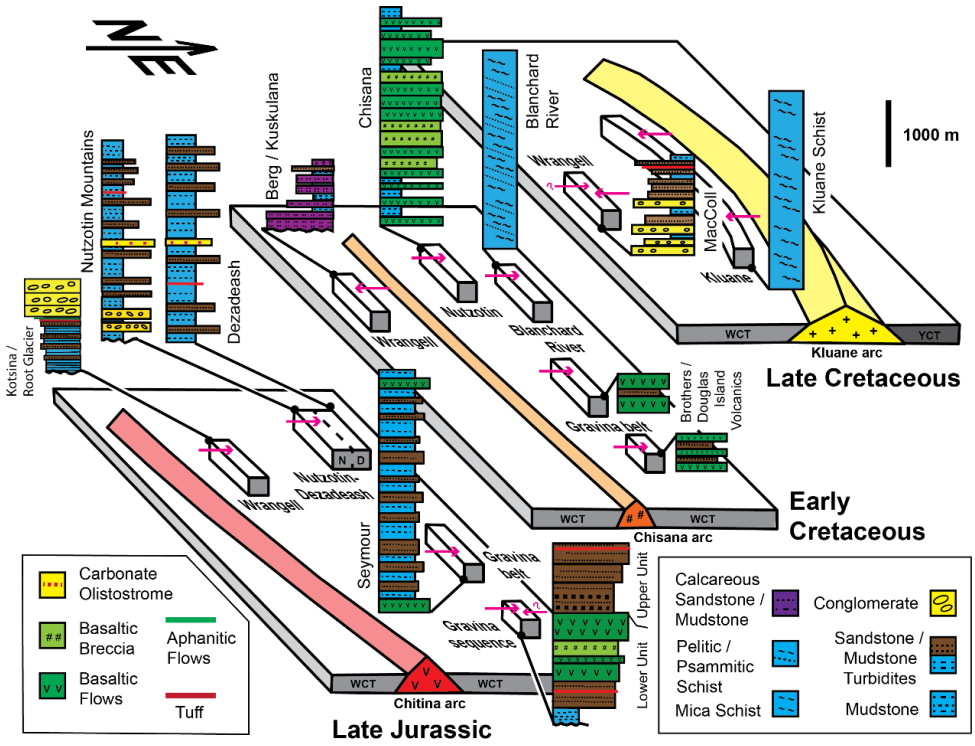

Fig. 2. Conceptual diagram depicting the spatial-temporal relationships of magmatic arcs (i.e., Chitina, Chisana, and Kluane) and associated basins (i.e., Wrangell, Nutzotin-Dezadeash, Gravina belt, Gravina sequence, Blanchard River assemblage, and Kluane Schist). Only movement on the Denali fault (dashed line separating Nutzotin-Dezadeash basin) has been restored. Small (pink) arrows indicate general paleoflow directions.

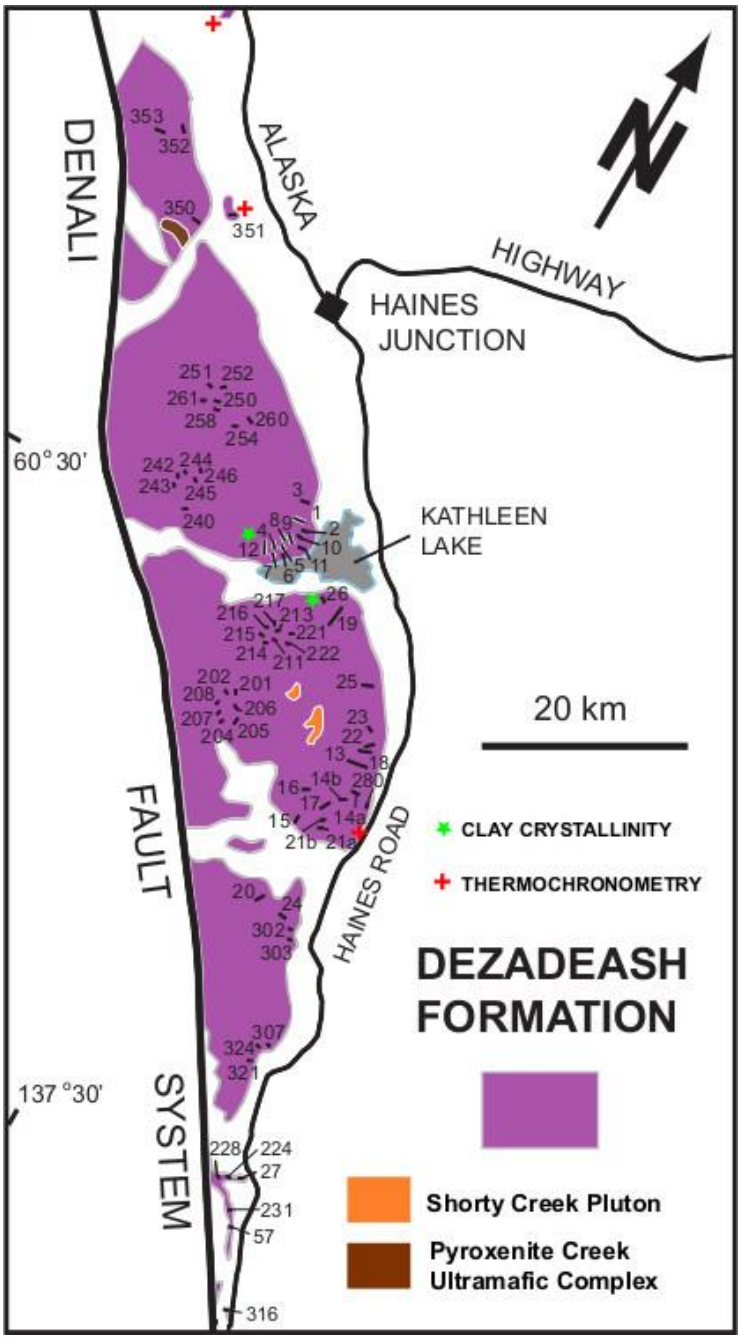

Fig. 3. Location of measured sections (numbers) in the Dezadeash Formation, Yukon, from which samples were collected. Also shown is location of published thermochronometric data for the Dezadeash Formation (see text for details).

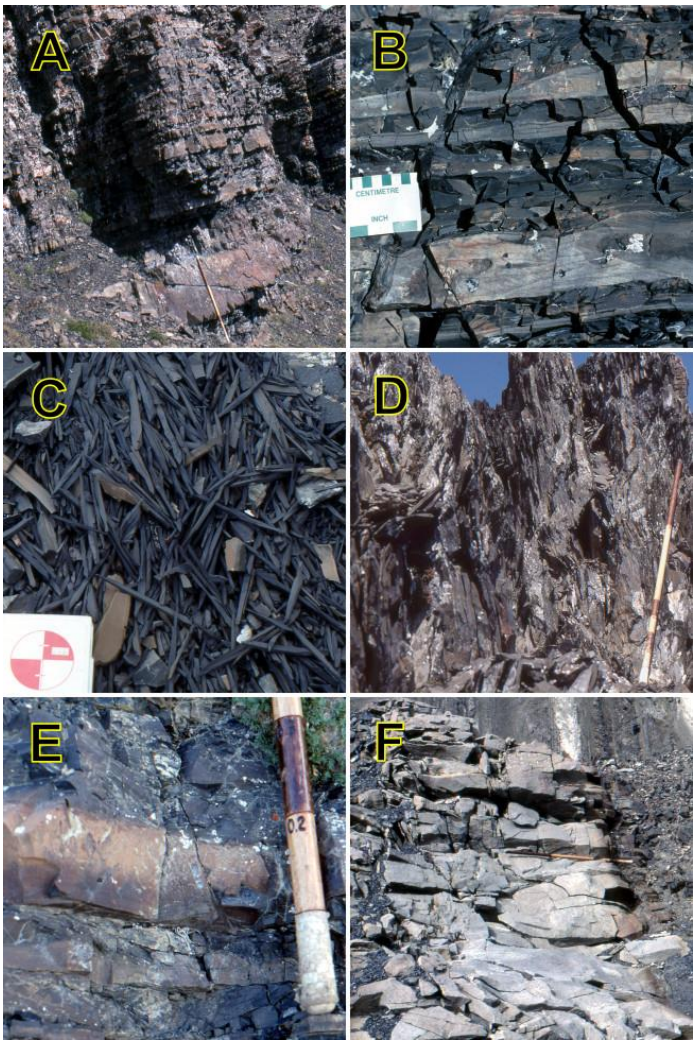

Fig. 4. Photographs of representative secondary structures in the Dezadeash Formation, Yukon. (A) Parting (sub-vertical) in thin- to medium-bedded sandstone-mudstone couplets, 1.5m long Jacob's Staff for scale. (B) Parting (sub-vertical) in thin-bedded sandstone-mudstone couplets, green squares at top of scale card are 1cm long. (C) Spaced cleavage (vertical) in mudstone, 1.5m long Jacob's Staff for scale. (D) Pencil structure in mudstone, length of black bar in circle on notebook is 6 cm. (E) Parting (vertical) in hemipelagite bed (brown bed), dark brown interval on Jacob's Staff is 0.1m long. (F) Parting (horizontal) in tuff bed, 1.5m long Jacob's Staff for scale.

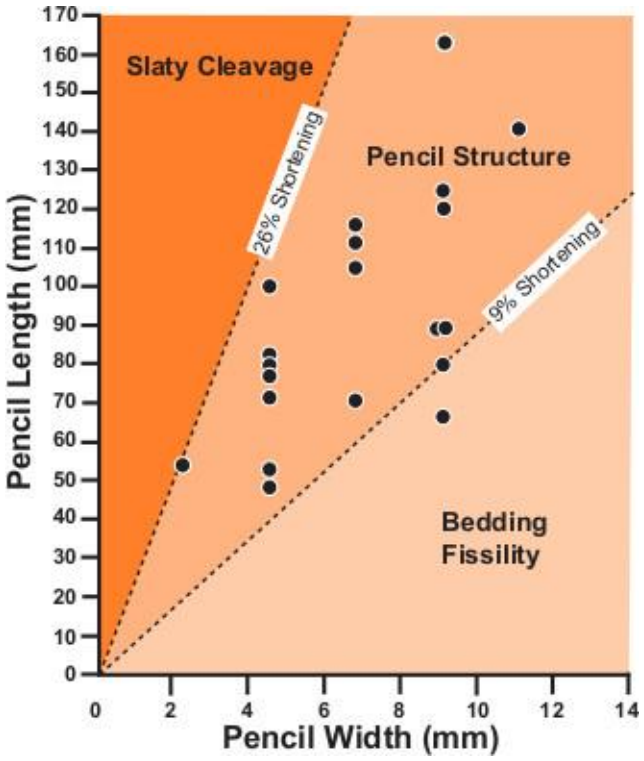

Fig. 5. Plot of pencil width vs. length of mudstone samples from the Dezadeash Formation, Yukon (diagram after Passchier and Trouw, 1996).

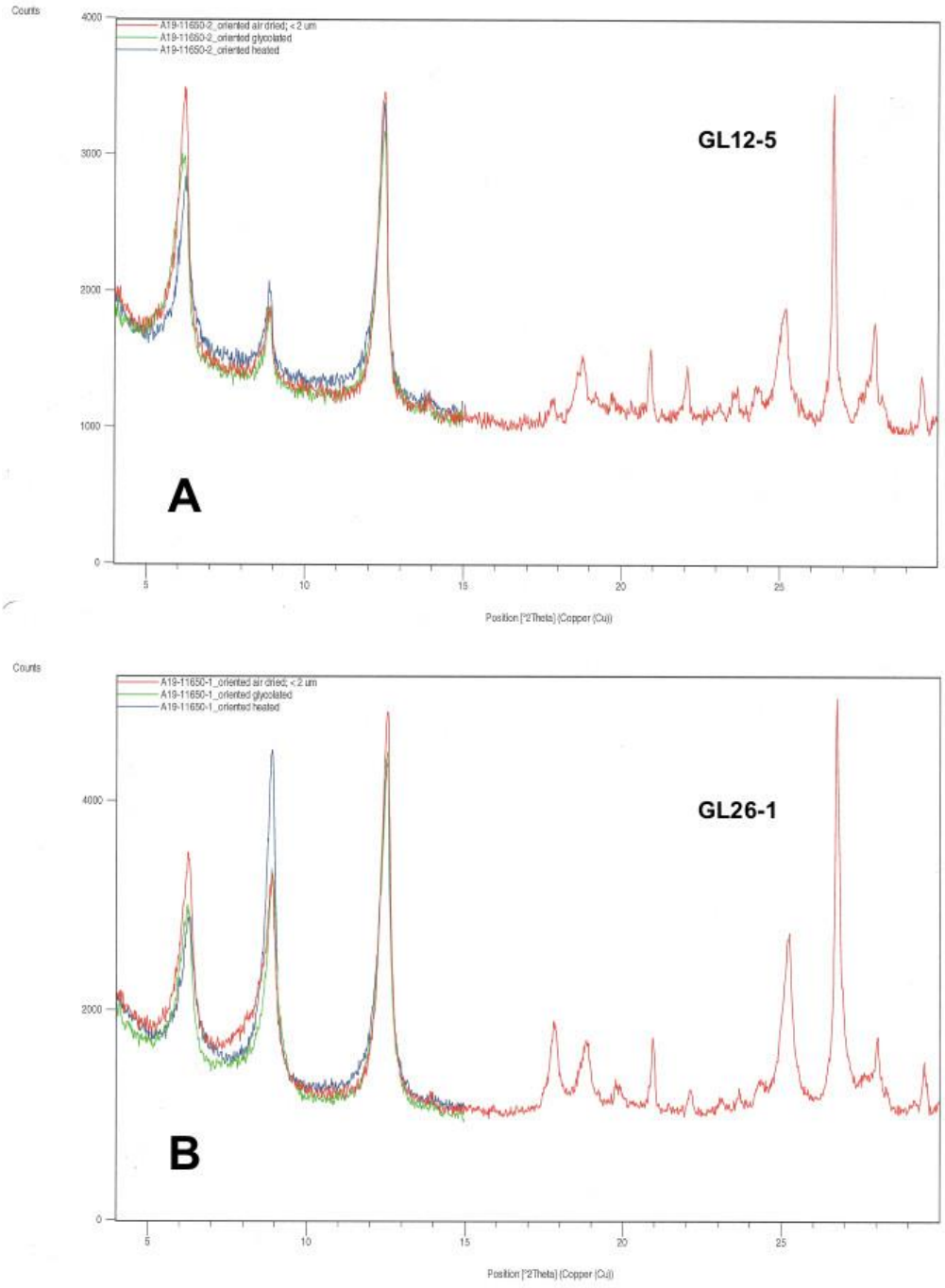

Fig. 6. X-ray diffractograms of mudstone samples from the Dezadeash Formation, Yukon. (A) GL12-5. (B) GL26-1.

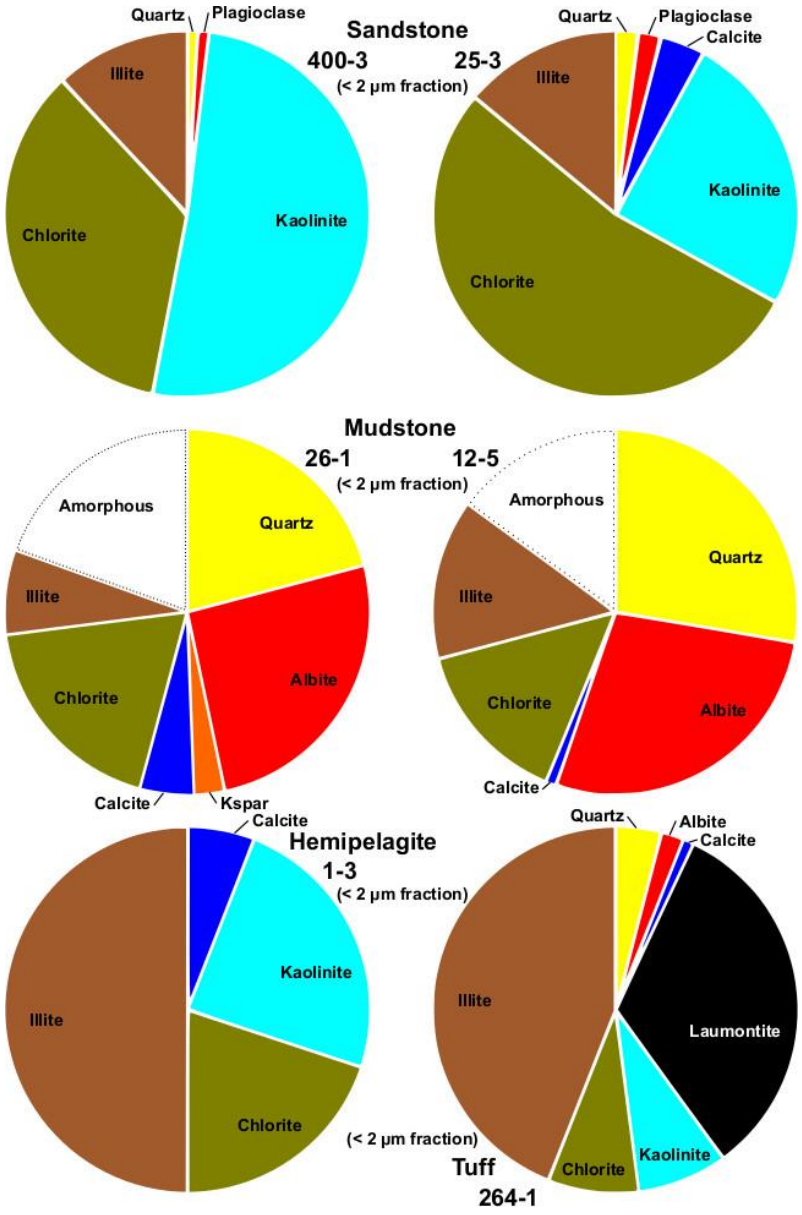

Fig. 7. Pie diagrams of clay-size fraction (< 2 µm) in sandstone, mudstone, hemipelagite, and tuff samples from the Dezadeash Formation, Yukon.

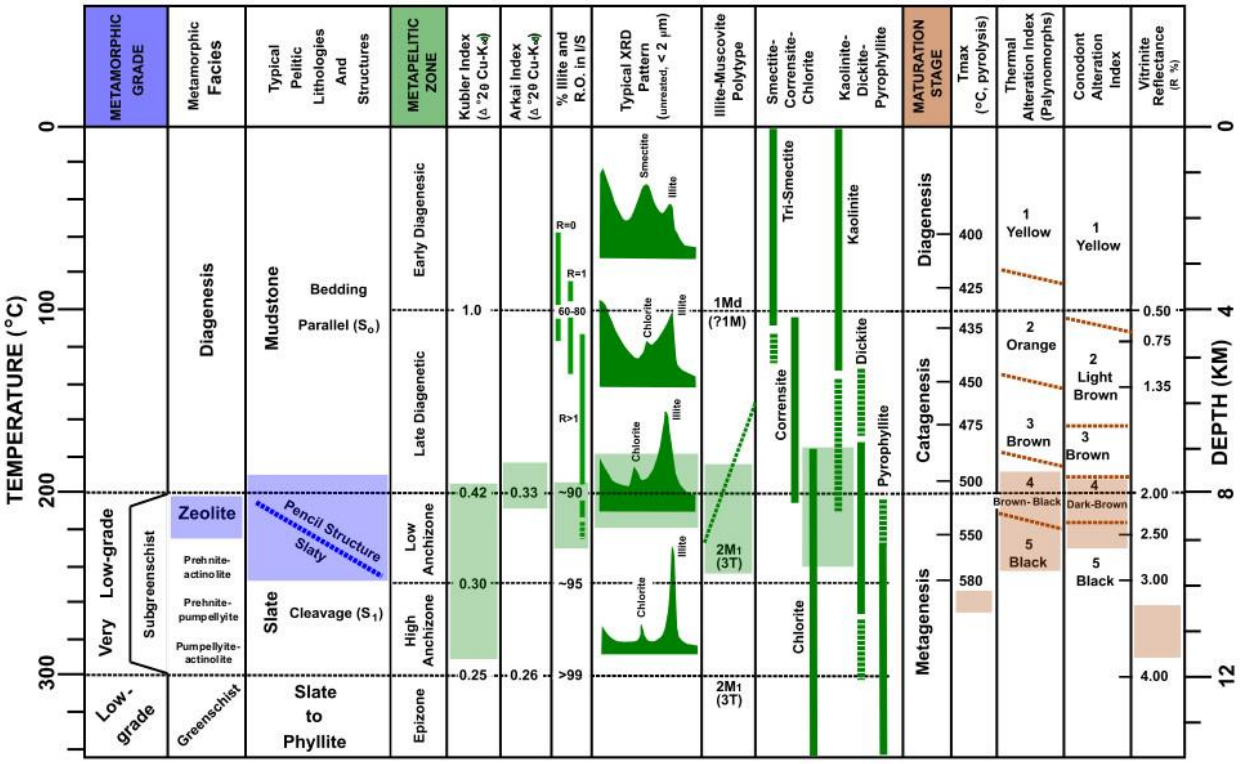

2231

2232

2233 Fig. 8. Correlation diagram of metamorphic grade, metapelitic zone, and maturation stage for the

2234 Dezadeash Formation, Yukon. Note that temperature and depth are only approximate. Compiled

2235 from Héroux et al. (1979), Bird et al. (1999), and Hartkopf-Fröder et al. (2015).

2236

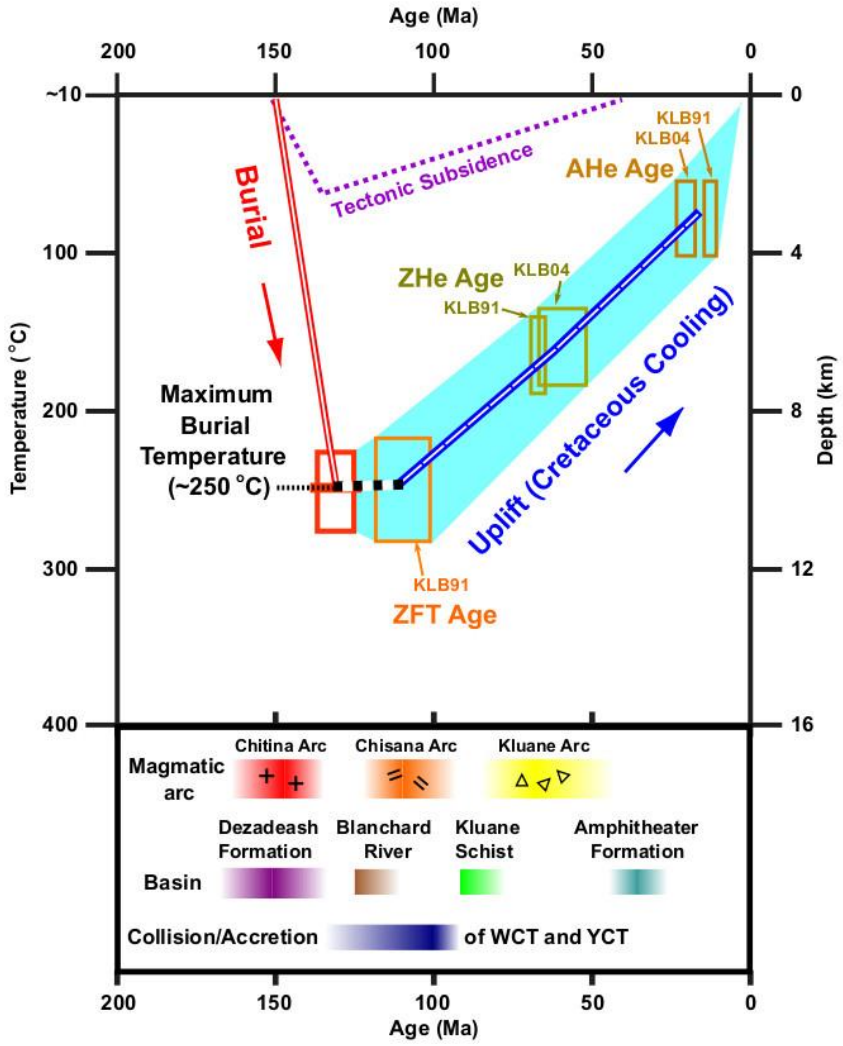

Fig. 9. Time vs. temperature diagram for the Dezadeash Formation, Yukon. Thermochronometric samples KBL04 and KBL91 from Enkelmann et al. (2017). Size of the boxes for thermochronometric samples indicate uncertainties in age and temperature estimates.

Table S1. Section locations (along which samples were collected), Dezadeash Formation, Yukon, Canada.

Section	NTS Map		Easting	Northing		Easting	Northing
1	115 A/11	Start	371000	6719500	End	369200	6718000
2	115 A/11	Start	371600	6718700	End	371200	6718600
3	115 A/11	Start	370400	6720800	End	369200	6720500
4	115 A/11	Start	369700	6716600	End	369200	6716200
5	115 A/11	Start	369700	6716500	End	369400	6716700
6	115 A/11	Start	370500	6716300	End	370300	6716600
7	115 A/11	Start	369500	6715600	End	369300	6716000
8	115 A/11	Start	370300	6717000	End	369400	6717500
9	115 A/11	Start	370600	6717800	End	369800	6718300
10	115 A/11	Start	370900	6718300	End	370400	6718200
12	115 A/11	Start	369300	6715700	End	368500	6716700
13	115 A/11	Start	385400	6702500	End	383600	6702300
14A	115 A/11	Start	385500	6699300	End	384800	6699200
14B	115 A/11	Start	384700	6698800	End	384300	6698700
16	115 A/11	Start	381200	6698200	End	380700	6698200
17	115 A/11	Start	383300	6696900	End	384200	6697700
18	115 A/11	Start	385100	6703900	End	384100	6703800
19	115 A/11	Start	377000	6715000	End	376200	6714300
20	115 A/11	Start	382500	6687700	End	382300	6687300
21B	115 A/11	Start	384300	6695700	End	384300	6695700
22	115 A/11	Start	384700	7604600	End	384500	6705000
23	115 A/11	Start	384300	6705400	End	383800	6705900
24	115 A/11	Start	384700	6684700	End	384500	6684800
25	115 A/11	Start	382200	6709300	End	381400	6708700
26							
27	115 A/2	Start	392000	6665100	End	392000	6665100
201	115 A/6	Start	371800	6701400	End	371800	6701400
208	115 A/6	Start	371200	6701400	End	371200	6701400
219	115 A/6	Start	373000	6708700	End	373000	6708700
244	115 A/12	Start	358200	6717500	End	358200	6717500
247	115 A/12	Start	359400	6717700	End	359400	6717700
250	115 A/12	Start	358500	6725000	End	358500	6725000
257	115 A/12	Start	358600	6724700	End	358600	6724700
260	115 A/12	Start	361600	6724500	End	360700	6725300
280 (74B, 400)	116 A/6	Start	387094	6608552	End	387094	6608552
351 (74A)	115 A/12	Start	352956	6740958	End	352956	6740958
352	115 A/13	Start	344400	6745700	End	344300	6745800

Supplementary Table S2. X-ray diffraction analyses, Dezadeash Dormation, Yukon, Canada.

Sample	Lithology	Grain-size	Weight (%)	Quartz (%)	Plagioclase (%)	Kspar (%)	Calcite (%)	Muscovite (%)	Laumontite (%)	Siderite (%)	Kaolinite (%)	Chlorite (%)	Illite (%)	Other (%)	Clay Minerals (%)	Total (%)
25-3	Sandstone	Bulk (Coarse+Clay)	100.00	22	25	0	12	4	0	0	15	20	2		37	100
		Coarse (>2µm)	90.88	24	28	0	12	5	0	0	14	17	0		31	100
		Clay (<2µm)	9.12	2	2	0	4	0	0	0	**25**	**53**	**14**		**92**	100
400-3	Sandstone	Bulk	100.00	24	37	0	2	2	0	0	11	15	9		34	100
		Coarse	94.96	25	40	0	2	2	0	0	8	55	8		31	100
		Clay	5.04	1	1	0	0	0	0	0	**51**	**35**	**12**		**98**	100
1-3	Hemipelagite	Bulk	100.00	12	5 (Albite)	< 0.1	63	2	0	0	8	8	2	Pyrite	18	100
		Coarse	96.00	13	5	< 0.1	66	2	0	0	7	7	0	Bassanite	15	100
		Clay	4.00	0	0	0	6	0	0	0	**24**	**20**	**50**		**94**	100
264-1	Tuff	Bulk	100.00	37	7 (Albite)	0	6	3	41	3	0.5	0.5	2		2	100
		Coarse	94.93	37	7	0	7	4	42	3	0	0	0		0	100
		Clay	5.07	4	2	0	1	0	33	0	**8**	**8**	**44**		**60**	100
12-5	Mudstone	Bulk	-	-	-	-	-	-	-	-	-	-	-	<10% expandable clay	-	-
		Coarse	-	-	-	-	-	-	-	-	-	-	-	KI=0.42, AI=0.34	-	-
		Clay	100	29.8	21.9 (Albite)	<0.1	1.0	-	-	-	**0**	**15.9**	**15.3**	Amorphous (16.1%)	**31.2**	100
26-1	Mudstone	Bulk	-	-	-	-	-	-	-	-	-	-	-		-	-
		Coarse	-	-	-	-	-	-	-	-	-	-	-	KI=0.26, AI=0.33	-	-
		Clay	100	20.9	25.8 (Albite)	2.7	4.8	0	0	0	**0**	**18.8**	**7.5**	Amorphous (19.5%)	**26.3**	100

KI=Kübler Index (units of Δ°2θ)
AI=Árkai Index (units of Δ°2θ)

Supplementary Table S3. Palynological analysis of mudstone and hemipelagites, Fezadeash Formation, Yukon, Canada.

Sample	Lithology	Spores	Pollen	AOM	Phytoclasts	Other
1-1	Mudstone	Trilete, dark brown, corroded	Monosulcate grain, dark brown, corroded	Black debris, round particles, dark brown to black, semi-opaque or opaque; Irregular 'fluffy' masses, dark brown and partly translucent; Globular masses, dark brown, degraded *Botryococcus* colonies ?	Black phytoclasts	Pyrite
1-2	Mudstone	Barren	Bisaccate grain, dark brown to black, corroded	black debris, round particles, dark brown to black, semi-opaque or opaque; irregular 'fluffy' masses, dark brown and partly translucent		
1-3	mudstone	Barren	Monosulcate grain, black, corroded	black debris, round particles, dark brown to black, semi-opaque or opaque		
1-4	mudstone	Trilete, dark brown, corroded	barren	black debris, round particles, dark brown to black, semi-opaque or opaque; irregular 'fluffy' masses, dark brown and partly translucent	black phytoclasts (leaf cuticles?)	
1-5	hemipelagite	Barren	Barren	black debris, round particles, dark brown to black, semi-opaque or opaque; irregular 'fluffy' masses; dark brown and partly translucent	black phytoclasts (leaf cuticles?)	pyrite
GL1-6	hemipelagite	Barren	Barren	black debris, round particles, dark brown to black, semi-opaque or opaque		pyrite
GL1-7	hemipelagite	Barren	Barren	black debris, round particles, dark brown to black, semi-opaque or opaque		
GL1-8	hemipelagite	Barren	Barren	black debris, round particles, dark brown to black, semi-opaque or opaque		

2247 AOM=amorphous organic matter. Thermal Alteration Index (TAI)= ~4.5.

Table S3. Microfossil analysis of carbonate boulder, Dezadeash Formation, Yukon, Canada (modified from Orchard, 2000).

Sample	Fossils	Age	CAI
247-1	ichthyoliths microbivalves foraminifer conodonts: ramiform elements *Neogondolella steinbergensis* (Mosher, 1968) *Epigondolella bidentata* (Mosher 1968)	Late Triassic (Late Norian)	4–4.5

2248

Table S5. Rock-Eval data, Dezadeash Formation, Yukon, Canada.

Sample	**Lithology**	**TOC** (wt%)	**T_{max}** (°C)	**S_1** (mg HC/g rock)	**S_2** (mg HC/g rock)	**S_3** (mg CO_2/ g rock)	**HI**	**OI**
1-3	Hemipelagite	0.03	437	0.01	0.06	0.24	200	800
2-2	Hemipelagite	0.17	451	0.00	0.02	0.35	12	206
3-2	Hemipelagite	0.20	442	0.07	0.03	0.35	15	175
3-9	Hemipelagite	0.12	481	0.00	0.00	0.50	0	413
4-2	Hemipelagite	0.06	-40	0.01	0.00	0.21	0	350
4-7	Hemipelagite	0.15	285	0.16	0.03	0.36	20	240
4-8	Mudstone	1.26	589	0.04	0.06	0.41	5	33
8-5	Hemipelagite	0.08	362	0.01	0.00	0.23	0	288
9-4	Mudstone	0.15	342	0.00	0.00	0.35	0	233
9-6	Hemipelagite	0.17	406	0.01	0.00	0.54	0	318
12-4	Hemipelagite	0.10	428	0.01	0.00	0.38	5	380
12-5	Mudstone	0.19	314	0.12	0.01	0.28	0	147
16-1	Mudstone	0.14	-40	0.00	0.00	0.31	20	221
18-1	Sandstone	0.05	487	0.00	0.01	0.30	0	600
18-4	Hemipelagite	0.04	-40	0.00	0.00	0.42	0	1050
22-1	Mudstone	0.07	421	0.00	0.00	0.35	14	500
23-1	Sandstone	0.07	428	0.00	0.01	0.24	0	343
26-1	Hemipelagite	0.07	430	0.00	0.00	0.27	0	386
28-1	Phyllite	0.01	-40	0.00	0.00	0.28	0	2800
203-1	Mudstone	0.11	-40	0.00	0.00	0.30	0	273
210-1	Hemipelagite	0.25	433	0.00	0.00	0.27	0	108
213-1	Mudstone	0.08	-40	0.00	0.00	0.26	0	325
307-1	Mylonite	0.09	362	0.01	0.00	0.77	0	856

TOC=total organic carbon
T_{max}=Rock-Eval oven temperature at maximum S_2 generation
S_1=hydrocarbons thermally distilled from sample ('free hydrocarbons')
S_2=hydrocarbons generated by pyrolytic degradation of kerogen in sample ('potential hydrocarbons')
S_3=carbon dioxide generated during pyrolysis
HI=Hydrogen Index=(S_2x100/TOC)
OI=Oxygen Index=(S_3x100/TOC)
HC=hydrocarbons

2249